Analysis of HMQC experiments applied to a spin-1/2 nucleus subject to very large CSA

Piotr Paluch, Andrew G. M. Rankin, Julien Trebosc, Olivier Lafon, Jean-Paul Amoureux

Analysis of HMQC experiments applied to a spin ½ nucleus subject to very large CSA

Piotr Paluch,[*1,,2] *Andrew G.M. Rankin,*[2] *Julien Trébosc,*[2] *Olivier Lafon,*[2,4] *Jean-Paul Amoureux*[*2,3]

[1] Centre of Molecular and Macromolecular Studies, Polish Academy of Sciences, Sienkiewicza 112, PL-90 363 Lodz, Poland.
[2]Univ. Lille, CNRS 8181, UCCS: Unit of Catalysis and Chemistry of Solids, F-59000 Lille, France.
[3] Bruker Biospin, 34 rue de l'Industrie, F-67166 Wissembourg, France.
[4] Institut Universitaire de France, 1 rue Descartes, F-75231 Paris Cedex 05, France.

*Corresponding authors
Piotr Paluch: ppaluch@cbmm.lodz.pl, piotr.paluch@gmail.com
Jean-Paul Amoureux: jean-paul.amoureux@univ-lille.fr

Keywords: ^{195}Pt, solid-state NMR, *D*-HMQC, large CSA, inverse ^{1}H detection, selective excitation, DANTE.

Abstract. The acquisition of solid-state NMR spectra of "heavy" spin I = 1/2 nuclei, such as ^{119}Sn, ^{195}Pt, ^{199}Hg or ^{207}Pb can often prove challenging due to the presence of large chemical shift anisotropy (CSA), which can cause significant broadening of spectral lines. However, previous publications have shown that well-resolved spectra can be obtained *via* inverse ^{1}H detection using HMQC experiments in combination with fast magic angle spinning. In this work, the efficiencies of different ^{195}Pt excitation schemes are analyzed using SIMPSON numerical simulations and experiments performed on cis- and transplatin samples. These schemes include: hard pulses (HP), selective long pulses (SLP) and rotor-synchronized DANTE trains of pulses. The results show that for spectra of species with very large CSA, HP is little efficient, but that both DANTE and SLP provide efficient excitation profiles over a wide range of CSA values. In particular, it is revealed that the SLP scheme is highly robust to offset, pulse amplitude and length, and is simple to set up. These factors make SLP ideally suited to widespread use by "non-experts" for carrying out analyses of materials containing "heavy" spin I = 1/2 nuclei that are subject to very large CSAs. Finally, the existence of an "intermediate" excitation regime, with an rf-field strength in between those of HP and SLP, which is effective for large CSA, is demonstrated. It must be noted that in some samples, multiple sites may exist with very different CSAs. This is the case for ^{195}Pt species with either square-planar or octahedral structures, with large or small CSA, respectively. These two types of CSAs can only be excited simultaneously with DANTE trains, which scale up the effective rf-field. Another way to obtain all the information is to perform two different experiments: one with SLP and the second with HP to excite the sites with moderate/large and small/moderate CSAs, respectively. These two complementary experiments, recorded with two different spinning speeds, can also be used to discriminate the center-band resonances from the spinning sidebands.

I. Introduction

Approximately one quarter of all NMR active nuclei have a spin quantum number equal to 1/2. Generally, such nuclei are easier to detect than those with spin value larger than 1/2. This is because spin-1/2 nuclei have no electric quadrupole moment, and hence are not subject to quadrupole interactions, which generally lead to significant line broadening in the liquid and solid states. As a result, all NMR active spin-1/2 nuclei are observable in the liquid state *via* direct detection for high abundance and high gyromagnetic ratio nuclei or *via* inverse detection in other cases. However, in the case of solid samples, dipolar coupling and chemical shift anisotropy (CSA) interactions are not cancelled out due to the absence of overall isotropic molecular motions. Homo-nuclear dipolar interactions are the main problem for the NMR observation of ^{1}H (and sometimes ^{19}F) in the solid state since they can cause significant line broadening. Two methods can be used to overcome this type of broadening: homo-nuclear decoupling [1,2] and ultrafast magic angle spinning (uf-MAS).[3] Recently, uf-MAS has become very popular due to commercial MAS probes that are able to spin at rotation rates in excess of $\nu_R \approx 110$ kHz. One of the most important areas where ^{1}H detection is extremely useful are the inversely-detected ^{1}H-{^{13}C} or ^{1}H-{^{15}N} 2D correlations applied to unlabeled small molecules or labelled biological samples. Several impressive results have been presented in both fields by Pruski,[4,5,6] Nishiyama,[6,7,8,9] Pintacuda,[10,11,12] and others.[3,13,14] Such experiments are usually based on transfers with either double dipolar cross-polarization,[4,6-10] or with *J*-scalar couplings *via* the R-INEPT (Refocused Insensitive Nuclei Enhanced by Polarization Transfer) experiment.[5] As a result, presently most spin-1/2 nuclei can be considered to be relatively easy to detect in solid-state NMR, without any labelling. These "easy" nuclei (i) are subject to small or moderate CSA, which can easily be cancelled by conventional MAS or uf-MAS, (ii) are not subject to any paramagnetic interaction, and (iii) have a relatively small chemical shift range. On the other hand, less common but still very important spin-1/2 nuclei possess both extremely large CSA and chemical shift ranges (in ppm). These nuclei are typically transition metals and heavy nuclei (*e.g.* ^{119}Sn, ^{195}Pt, ^{199}Hg, ^{207}Pb).[15] It must be noted that some of them have small gyromagnetic ratios (*e.g.* ^{57}Fe, ^{103}Rh, ^{107,109}Ag, ^{183}W), which reduce their CSA and isotropic chemical shift ranges when expressed in frequency (in Hz). One example of a "difficult" heavy nucleus is ^{195}Pt, for which the CSA and chemical shift ranges can be as large as 13,000 ppm,[16] which strongly complicate the detection of this nucleus. Even the highest available MAS frequencies, presently in the range of $\nu_R \approx 120$ kHz, cannot average out such large CSA values. Moreover, due to the limited rf-field of commercial probes, short hard pulses (HP) are unable to effectively excite the whole range of chemical shifts and CSAs. Several methods have been proposed in the literature to overcome the problem of excitation and detection of very broad spectra. They use a single (WURST-CPMG)[17] or two channels (BRAIN-CP) excitation,[18] which can be combined with DNP,[19] or methods involving VOCS (Variable Offset Cumulative Spectra)[20] or CP transfers combined with CPMG (Carr-Purcell-Meiboom-Gill).[21] A comprehensive review of these methods has recently been published by Schurko.[22] Such methods work very well in the case of static samples or under moderate spinning speeds, but they are ineffective in the case

of uf-MAS, which limits their usefulness with respect to ^{1}H inverse detection sequences. Recently, Rossini *et al*. proposed two ^{1}H-{^{195}Pt} *D*-HMQC (Dipolar-based Heteronuclear Multiple-Quantum Correlation) inverse detection MAS methods for wide-line spectra. In the first method, (i) the two $\pi/2$-pulses on the ^{195}Pt channel of the conventional HMQC sequence are replaced with two short HPs with a small flip angle to broaden the ^{195}Pt excitation, albeit with a decrease in the S/N ratio, and (ii) the full ^{195}Pt CSA MAS line-shape can be observed by desynchronizing the evolution time, t_1.[23] The second method, called "aMAT-*D*-HMQC", allows for the observation of only the MAS center-band of each species at its true chemical shift, free from any 'folding' effects that may occur with the conventional rotor-synchronized methods.[24] It should be noted that the *D*-HMQC technique is currently the most popular method for ^{1}H detected correlation experiments involving ^{14}N (spin I = 1), where similar problems of extremely broad line-shapes exist. A variety of applications of such ^{1}H-{^{14}N} methods have been presented by Brown,[25] Nishiyama,[7,8,26] and others.[27] Our solid-state NMR group has very recently carried out detailed analyses of ^{1}H-{^{14}N} *D*-HMQC 2D schemes,[28,29] but these results cannot be directly extrapolated to ^{1}H-{^{195}Pt}, or to any spin-1/2 heavy nucleus, due to the different natures of the quadrupole and CSA interactions. Only few articles have been published on the analysis of the *D*-HMQC technique applied to spin-1/2 nuclei with large CSA.[23,24,30] Therefore, it seemed judicious to conduct a detailed analysis of the behavior of ^{1}H-{X} *D*-HMQC experiments involving spin-1/2 nuclei subject to large CSAs *versus* the different possible excitation schemes. In this article, an extended theoretical study of ^{1}H-{^{195}Pt} *D*-HMQC experiments is presented, and is supported by experimental data obtained for the cis- and transplatin model compounds.

There are two different ways of recording an HMQC 2D spectrum. Indeed, the sampling along the indirect dimension can be either rotor-synchronized or not. In the first case, all sidebands are folded back into the indirect spectral width limited to ν_R. This largely enhances the signal to noise (S/N) ratio, but only one sideband is observed for each species. In the second case, which can either be the constant-time or the aMAT HMQC versions [23,24], a very large spectral width is required. This decreases the S/N, but it provides either the full sideband MAS patterns or only the center-band resonances, respectively. In the following, we mainly focus on an analysis of the results obtained with rotor-synchronized sequences, which are by far the most used methods. However, to help the readers to better understand how the three excitation schemes work, at the end of the article we show in Fig.14 the results of several 2D spectra with an unsynchronized indirect dimension.

uf-MAS is required (i) to directly observe high-resolution ^{1}H spectra, (ii) to limit the number of ^{195}Pt spinning sidebands, and (iii) to maximize the indirect spectral width of rotor-synchronized experiments. Therefore, all simulations and experiments of this article, except in Fig.13, were performed with ν_R = 62.5 kHz (T_R = 16 μs).

II. 1D simulations of rotor-synchronized *D*-HMQC methods

II.1. General considerations

In the simulations, the CSA is always defined in kHz, which avoids any reference to the magnetic field. One isolated ^{1}H-^{195}Pt spin-pair with a dipolar interaction of $D_{^{1}H\text{-}^{195}Pt}$ = -2 kHz was used throughout the simulations. In Figs.2-9, the H-Pt inter-nuclear vector was always fixed along the main axis of the ^{195}Pt CSA tensor. In the following, the efficiency of the ^{1}H-{^{195}Pt} *D*-HMQC method, Eff, is always normalized with respect to that of the same sequence using $SR4_1^2$ recoupling, with perfect Dirac $\pi/2$ and π pulses on the two channels, and without any CSA and offset on ^{1}H and ^{195}Pt. The CSA is defined with the span ($\Omega = \delta_{11} - \delta_{33}$) of the static spectrum with an axially symmetric tensor (η = 0). *D*-HMQC sequences can be divided into two groups according to the location of the dipolar recoupling scheme: either on the S (observed) or on the I (indirect) channel; in this case ^{1}H and ^{195}Pt, respectively. To be efficient, the recoupling sequence must be applied on the nucleus subject to the smallest anisotropic interaction, here ^{1}H, and so in this work we used the sequence shown in Fig.1a. It should be mentioned that when the two nuclei are subject to large anisotropic interactions, *e.g.* ^{11}B and ^{207}Pb, it is possible to use an adiabatic recoupling scheme on the I channel.[31] Concerning the ^{1}H channel, one of the most widely used dipolar recoupling schemes is $SR4_1^2$, which is a super-cycled version of the symmetry-based $R4_1^2$ sequence. $SR4_1^2$ offers several advantages: (i) it has a large dipolar scaling factor (κ = 0.25),[32] (ii) its Hamiltonian commutes among different spin-pairs, thus avoiding the problem of dipolar truncation, and hence allowing the observation of long inter-nuclear distances, (iii) it partially suppresses the ^{1}H-^{1}H interactions, limiting signal losses during the mixing times, and (iv) it is robust with respect to offset, CSA, pulse imperfections and rf-inhomogeneity.[33,34] It must be noted that very recently, two new recoupling sequences, $SR4_1^2$ (II) and $R12_3^5$ (II) have been proposed for ^{1}H-{X} *D*-HMQC experiments at uf-MAS. These two sequences replace the basic π-pulses with $90_{-45}90_{45}90_{-45}$ composite π-pulses to decrease the effects of ^{1}H-^{1}H interactions.[35] As a result, these sequences quench the spin diffusion and hence long-lived recoupled coherence lifetimes can be obtained, which facilitate the detection of cross-peaks related to small dipolar interactions. Other schemes such as SFAM (Simultaneous Frequency and Amplitude Modulations),[34,36] can be used when the S nucleus is not ^{1}H.

In this article, we have used the $SR4_1^2$ recoupling with basic π-pulses because the ^{1}H-^{195}Pt dipolar interaction is generally not small (2 kHz here). The $SR4_1^2$ scheme is rotor-synchronized, which means that the duration of each refocusing part must be a multiple of the rotor period, T_R. Moreover, $SR4_1^2$ is not γ-encoded, which means that the beginning of the excitation and refocusing periods must be rotor-synchronized. Globally, this means that the beginnings and ends of the two recoupling blocks must be rotor synchronized. In the simulations, the ^{1}H $\pi/2$ and π pulses were defined to be perfect Dirac pulses, and the rf-field of the $SR4_1^2$ recoupling was fixed at its theoretical optimum value of $2\nu_R$.

The results shown in Figs.2-5,8 with single-pulse excitation were obtained with the sequence shown in Fig.1a by fixing t_1 = 32 μs. This delay is required because (i) the length of each of the two pulses on ^{195}Pt channel was increased up to $2T_R$ = 32 μs, (ii) t_1 is defined between the

middles of these two pulses, and (iii) rotor-synchronized experiments were analyzed. Those with D_1^k excitation shown in Fig.6-8 used $t_1 = kT_R$ to take into account the DANTE length of kT_R. Concerning the two excitation blocks on the I = ^{195}Pt channel, t_p is designated as the length of each individual pulse, and ν_1 is its rf-amplitude.

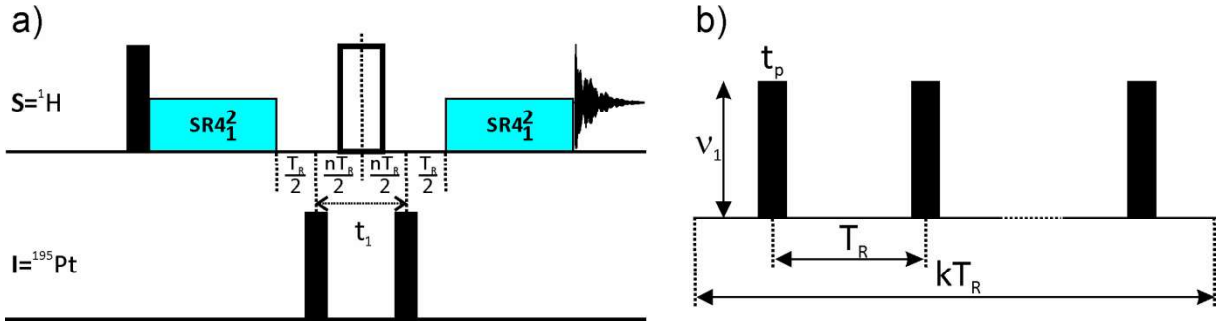

Fig.1. (a) Rotor-synchronized *D*-HMQC sequence with recoupling on the S = ^{1}H observed channel. (b) Schematic outline of the D_1^k DANTE excitation scheme.

The HMQC scheme was originally proposed for liquid samples and was composed of four pulses: a $\pi/2$ and a π-pulse on the S channel and two $\pi/2$-pulses on the I channel bracketing the evolution period, t_1. In the case of ^{1}H-{^{195}Pt} HMQC simulations concerning solid samples, the two S pulses can be replaced with two perfect Dirac pulses because the ^{1}H CSA and chemical shift ranges are quite limited. This is the contrary with respect to the large CSA interaction on the ^{195}Pt channel. Therefore, each of the two $\pi/2$ pulses on I can be replaced with one excitation that could be provided with either a hard-pulse (HP), a selective long-pulse (SLP), a DANTE train of pulses (D_1^k), a composite pulse, or an amplitude or phase-modulated excitation. In this work, our analysis is focused on the behavior of the first three excitation schemes. In the simulations the carrier frequency was fixed at the ^{195}Pt isotropic chemical shift, except in Figs.5 and 7 where the robustness to offset has been analyzed. It must be noted that the name of 'selective long pulse' may appear slightly misleading because, as we will see below, this pulse is robust towards offsets. This is contrary to the way selective long pulses are used in liquids. However, in Figs.9 and 14 we demonstrate that in MAS, and contrary to HP and D_1^k pulses that excite numerous sidebands, SLP only excites the sideband that coincides with the carrier frequency. As a result, SLP can hence be considered as selective when only observing the sideband combs.

II.2. Simulation results with two single pulses

In this section, the behavior of the ^{1}H-{^{195}Pt} *D*-HMQC sequence featuring two rectangular single pulses (SP) on the ^{195}Pt channel is analyzed. The pulse length is changed in the range of t_p = 0-32 μs. The results are displayed as series of two-dimensional (2D) maps that plot the efficiency with color scales.

II.2.a Efficiency *versus* (t_p & ν_1)

We have first examined the on-resonance efficiency *versus* the pulse length and amplitude (t_p, ν_1), for 8 span values of Ω = 0, 300, 600, 900, 1200, 1500, 2250 and 3000 kHz. These simulations expand upon previous work performed with Ω = 1000 kHz [29,30].

In the absence of CSA, the maximum intensity is obtained for flip angles $\theta = 2\pi\nu_1 t_p = (2n+1)\pi/2$ (90, 270, 450°, *etc.*) (Fig.**2a**). This is the hard pulse (HP) behavior typically observed for spin-1/2 nuclei when the CSA is much lower than ν_R and ν_1. Indeed, in this case the signal is proportional to $\sin^2(\theta)$, as expected from the two S $\leftrightarrow$ I transfers.

When non-zero values of CSA are considered, the excitation behavior is more complicated. With small to moderate CSA (*i.e.*, $\Omega \leq$ 600 kHz) (Fig.**2b**,**c**), it is only possible to obtain a maximum intensity for $\theta \approx \pi/2$, regardless of the pulse duration or amplitude. However, it should be noted that this area is not uniform, as it is with Ω = 0, and it becomes less intense when ν_1 is low. With moderate to large CSA ($\Omega \geq$ 900 kHz), only very short HPs with high rf-field, corresponding to $\theta \approx \pi/2$, are very effective and provide close to the maximum efficiency of Eff ≈ 1. However, it is important to note that the required rf-field increases substantially at higher CSA values; for example, with $\Omega \geq$ 1200 kHz, $\nu_1 \geq$ 200 kHz is required in order to maintain such efficiency. It can also be observed that it is possible to achieve an effective excitation (Eff ≈ 0.5-0.6) with a much lower rf-field and longer pulse duration. This selective long pulse (SLP) excitation starts being efficient for $\Omega \geq$ 600 kHz.

The HP scheme is based on the assumption of a simultaneous excitation of all crystallites, which is why the maximum possible rf-field strength must be used. In contrast, the SLP scheme is based on the rotor-driven sequential excitation of the crystallites, which occurs when the time-dependent CSA interaction becomes small as a result of sample rotation. This principle leads to the use of SLP with a moderate rf-field ($\nu_1 < \nu_R$) and an extended duration of *ca.* $T_R \leq t_p \leq 2T_R$. It must be noted that this regime corresponds to a broad region in the (t_p, ν_1) map, unlike the HP regime, which is quite narrow-banded. This broadness means that this condition is very robust with respect to rf-field miss-calibration and inhomogeneity, and that the experimental setup is relatively straightforward. From simulations at ν_R = 62.5 kHz, the optimal rf-field was found to be ca. $2\nu_R/3$ = 42 kHz and the optimal pulse duration ca. $1.5T_R$ = 24 μs, although a slight increase is observed along with increasing CSA. These optimal parameters are marked by a cross in Fig.**2**. Recent works have shown that the SLP scheme is also very efficient for ^{1}H-{^{14}N} experiments.[28,37]

There is another broad region where the excitation is also effective when Ω > 600 kHz. In this situation, $t_p < T_R$ and ν_1 is in between that of the HP and SLP regimes. This intermediate regime, with Eff ≈ 0.5, is clearly observed in Fig.**2f** with Ω = 1500 kHz for parameters of $t_p \approx$ 5 μs and $\nu_1 \approx$ 100 kHz, which correspond to $\theta \approx \pi$.

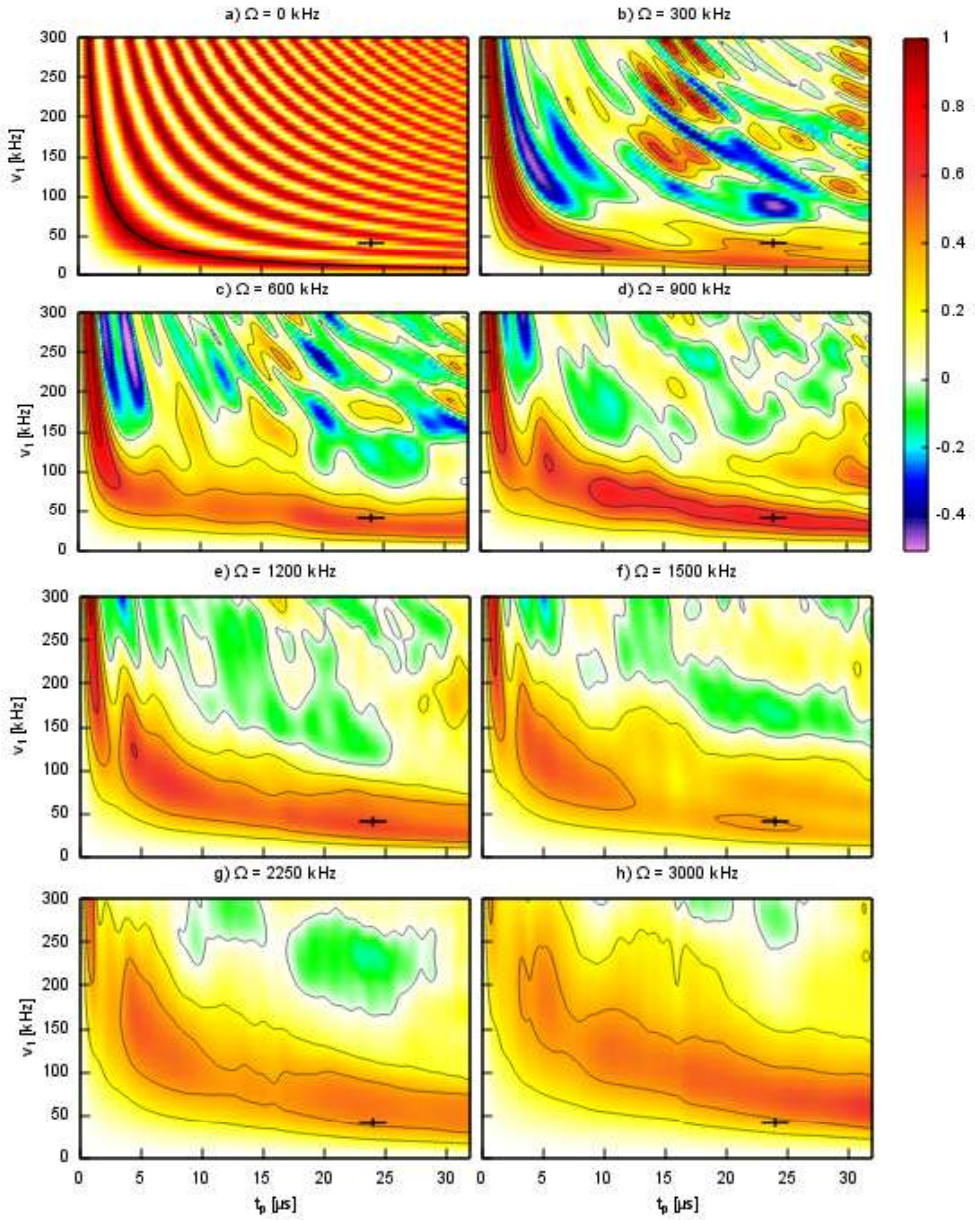

Fig.2. Simulated on-resonance efficiency of ^{1}H-{^{195}Pt} *D*-HMQC experiments *versus* the pulse duration (t_p) and amplitude (ν_1) for eight different Ω values indicated above each sub-figure. The contour levels were drawn in intensity increments of 0.2, and the corresponding color scale is shown on the right. Theoretical optimal values for SLP ($\nu_1 = 2\nu_R/3$ and $t_p = 1.5T_R$) are marked by a cross.

II.2.b Efficiency *versus* (ν_1 & Ω)

To further analyze the behavior of ^{1}H-{^{195}Pt} *D*-HMQC experiments, simulations were performed with four representative pulse durations selected according to previous simulations (t_p = 1.25, 2.5, 5 and 24 µs), *versus* the rf-field strength and CSA. The results are displayed in Fig.3.

As expected, and in agreement with previous results, the most intense signal is always observed with two $\pi/2$ HPs, but this efficiency strongly decreases when the CSA increases, especially when a low ν_1 value is used. This behavior may be rationalized by considering that

the excitation bandwidth of a $\pi/2$ pulse is inversely proportional to t_p. It follows therefore, that if the CSA pattern exceeds the excitation bandwidth, the signal intensity outside of this window is lost. The HP excitation is most effective for $\Omega \leq 300$, 600, 1200 kHz with t_p = 5, 2.5, 1.25 μs, or ν_1 = 50, 100, 200 kHz, respectively. It can also be seen that the intermediate regime with $\theta \approx 180°$ pulses is effective for $\Omega \geq 900$ kHz with $\nu_1 \approx 100$ kHz and t_p = 5 μs. This regime is less visible for t_p = 2.5 μs, but still exists with Ω > 2000 kHz. The efficiency of the SLP regime is observable in Fig.3**d**, where an effective excitation (Eff ≈ 0.5-0.6) is observed across a broad rf-range, centered around $\nu_1 \approx 2\nu_R/3$. It is important to note that this region broadens along the ν_1 axis when the CSA increases. This means that for large CSAs: (i) the full rotor sample is excited, hence increasing the S/N, and (ii) almost no experimental optimization is needed, making the scheme very simple to set up. Another benefit of this regime is that it requires a relatively low rf-field, and hence problems related to sample heating or probe detuning are unlikely to be encountered.

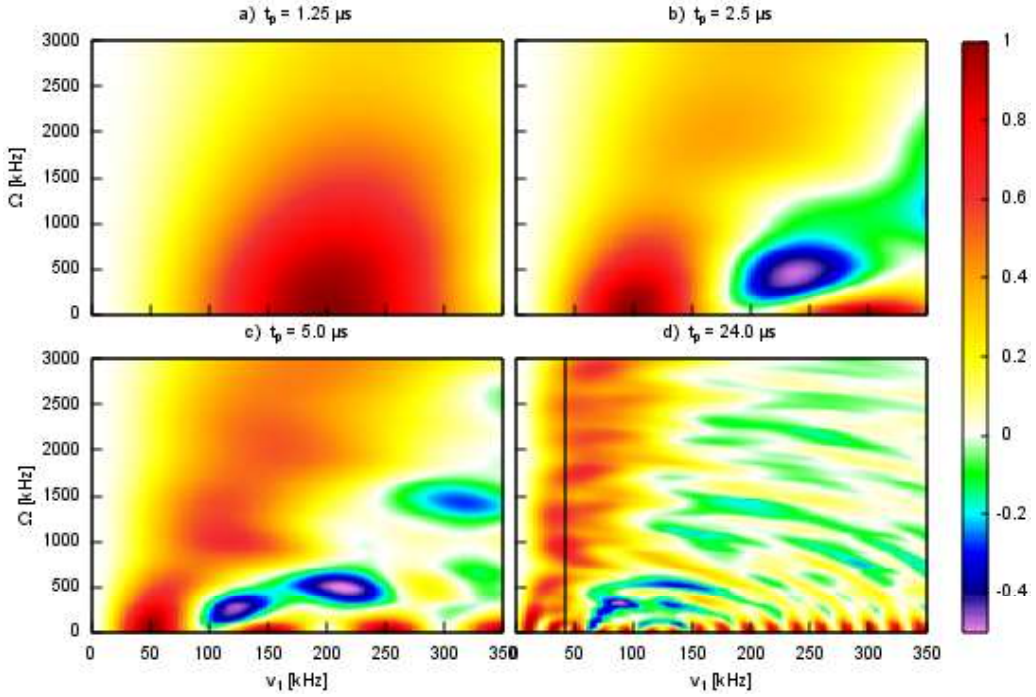

Fig.3. Simulated on-resonance efficiency of ^{1}H-{^{195}Pt} *D*-HMQC experiments *versus* (ν_1 & Ω) for four typical t_p pulse durations, as indicated of the subfigures. In (d), the condition $\nu_1 = 2\nu_R/3$ = 42 kHz is indicated by a black vertical line.

II.2.c Efficiency *versus* (t_p & Ω)

Practically, the choice of experimental parameters for ^{1}H-{^{195}Pt} *D*-HMQC experiments may be limited by the rf-capability of the probe. Accordingly, simulations of the efficiency were performed *versus* t_p and Ω with four selected rf-fields (ν_1 = 200, 100, 50 and 42 kHz), and the results are shown in Fig.**4**.

For the highest rf-field, ν_1 = 200 kHz (close to the safety limit of most 1.3 mm MAS probes), a high-efficiency region is visible at t_p = 1.25 μs, which corresponds to the HP regime of $\pi/2$ pulses (Fig.**4a**). There is no significant change in efficiency up to $\Omega \leq 1000$ kHz. However, the sharpness of the matching profile must be noted. This means that (i) a large part of the

full-rotor sample will be inefficient due to rf-inhomogeneity, and (ii) that probe detuning due to increased temperature resulting from the use of this high rf-power can lead to a strong efficiency decrease and a corresponding increase in t_1-noise.

For a moderate rf-field of ν_1 = 100 kHz, all previously described effects are visible in Fig.**4b**. Indeed, (i) for $\Omega \leq 600$ kHz, the most effective pulses are the $\pi/2$-HPs, (ii) for larger CSAs, this HP excitation is ineffective, but the intermediate regime with $t_p \approx 5$ µs is efficient for $750 \leq \Omega \leq 1500$ kHz, and (iii) the regime corresponding to SLPs is observable for $10 \leq t_p \leq 20$ µs and $\Omega \geq 750$ kHz. In Fig.**4d** with ν_1 = 42 kHz $\approx 2\nu_R/3$, the two first HPs and intermediate regimes disappear, whereas the SLP one is more clearly observable with $\Omega \geq 600$ kHz. This excitation scheme is efficient up to at least Ω = 3 MHz, and very robust with respect to the pulse length ($t_p \approx$ 15-30 µs) and rf-field, as can be seen by comparing Fig.**4c** and **d**. This means that most of the full rotor sample can be excited with this SLP regime, and that the experiment is very simple to set up. The only drawback of SLPs is that some modulations of efficiency are clearly visible in Fig.**4c**,**d** as a function of CSA.

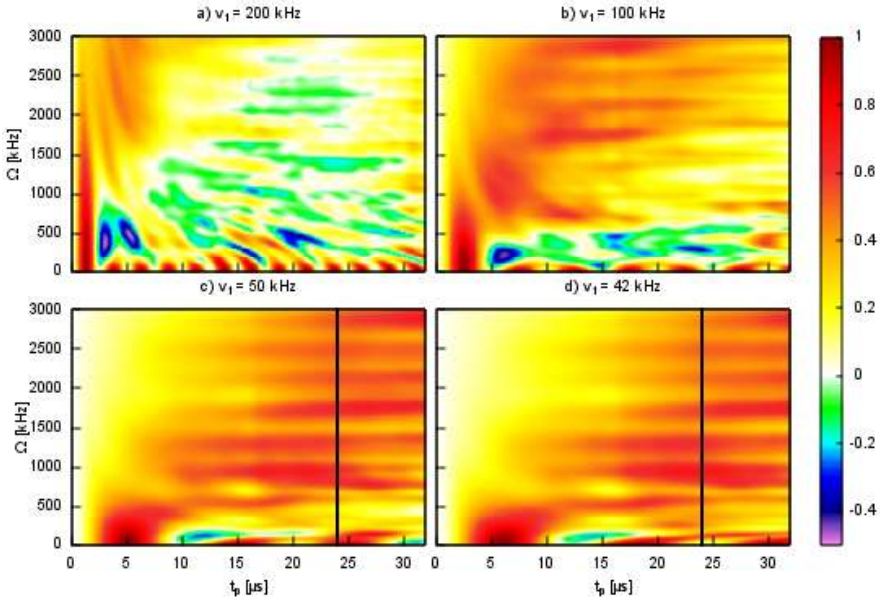

Fig.4. Simulated on-resonance efficiency of ^{1}H-{^{195}Pt} *D*-HMQC experiment *versus* t_p and CSA for four typical ^{195}Pt rf values as indicated in the subfigures. In (c) and (d) a vertical line at t_p = 24 µs indicates the recommended pulse length.

II.2.d Efficiency *versus* (offset & Ω)

Another important parameter is the robustness to offset, especially for nuclei such as ^{195}Pt, for which the chemical shift ranges can be as large as 13,000 ppm.[16,19] Fig.**5** shows the efficiency calculated *versus* offset and Ω for either two HPs with rf-fields of ν_1 = 100 and 200 kHz or two SLPs with ν_1 = 42 kHz. With two HPs, the robustness to both CSA and offset is proportional to ν_1, but it decreases inversely with respect to the CSA (Fig.**5a**,**b**). The opposite is true for SLPs, where robustness to offset increases concomitantly with CSA (Fig.**5c**). The modulations of efficiency versus CSA that were observed in Fig.**4c**,**d** are also clearly seen in Fig.**5c**.

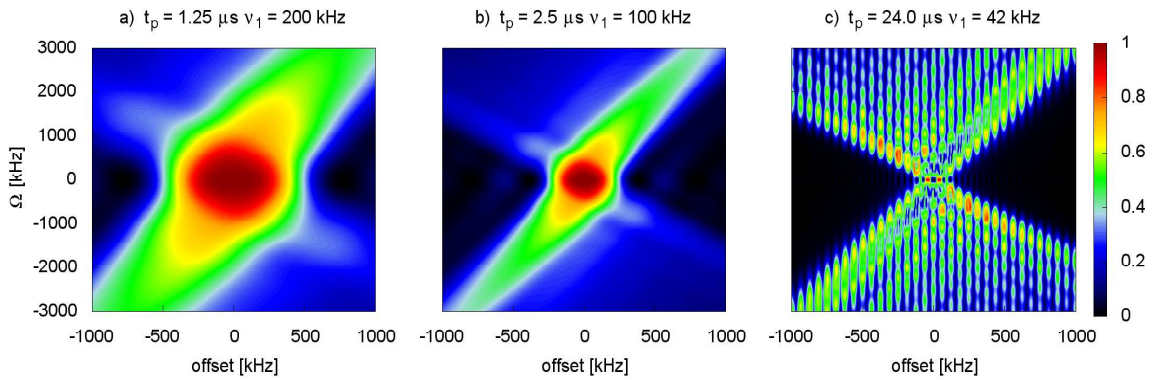

Fig.5. Simulated efficiency of ^{1}H-{^{195}Pt} D-HMQC experiments versus ^{195}Pt offset and span of the CSA for 3 typical rf-pulse durations and amplitudes (t_p (µs), ν_1 (kHz)) = (1.25, 200) (a), (2.5, 100 (b), (24, 42) (c). (a,b) The maximum signal is observed along an oblique line due to the axial symmetry of the CSA tensor.

II.3. Simulation results with two DANTE trains

It was previously mentioned that in the case of the *D*-HMQC sequence, the two rectangular $\pi/2$-pulses on the I (^{195}Pt) channel can be replaced by two composite, amplitude or phase-modulated shaped pulses. In this work the effects of DANTE excitations were analyzed. This excitation scheme was developed by Freeman et. al in the mid-1970s for selective excitation in solution state NMR spectroscopy.[38,39,40] However, in solid-state MAS NMR, DANTE pulses are actually used to *increase* the effective rf-field. The simplest version of this scheme consists of a train of k rotor-synchronized pulses, each with same duration of t_p, and separated by an interval of T_R, resulting in a total DANTE train duration of kT_R and a total flip-angle of $\theta = 2\pi\nu_1 kt_p$ (Fig.1b). The usual notation for such pulses is D_1^k. An interleaved DANTE sequence, referred to as D_N^k, has also been proposed, which consists of N interleaved basic D_1^k trains with N equally spaced pulses per rotor period.[41] In the present work however, only basic D_1^k trains were used.

The excitation profile of each $\mathbf{D_1^k}$ train is a comb of rf-spikelets, spaced by multiples of ν_R from the carrier frequency. In the case of the HMQC scheme with two $\mathbf{D_1^k}$ trains, the widths of each rf-**S**pikelet, S_{FWHM} and of their **E**nvelope, E_{FWHM} are respectively equal to:[29]

$$S_{FWHM} \approx 1.1/(kT_R) \text{ and } E_{FWHM} \approx 1.1/t_p \qquad (1)$$

It has been shown that with such $\mathbf{D_1^k}$ trains it is possible to efficiently excite very broad line-shapes, and that to a first approximation the effective rf-field is scaled up by the factor k with respect to ν_1.[41,42,43] $\mathbf{D_1^k}$ trains have been mainly used for the direct excitation of ^{19}F nuclei,[41-43] and for ^{1}H-{^{14}N} *D*-HMQC.[28]

A detailed analysis of the indirect detection of ^{14}N using DANTE has very recently been provided.[28] However, this spin-1 nucleus is subject to the quadrupole interaction (H_Q). Dephasing resulting from the first-order part of this interaction (H_{Q1}) must be minimized by utilizing a very stable spinning speed and ensuring that the magic angle is well adjusted, the so-called "STMAS requirements". The second-order part (H_{Q2}) introduces an attenuation of the signal during the D_1^k length of kT_R. However, spin-1/2 nuclei, such as ^{195}Pt, are not subject

to quadrupole interactions. Therefore, the effects related to the use of DANTE trains in ^{1}H-{X} *D*-HMQC experiments are different when X is a spin-1/2 (^{195}Pt) or a spin-1 (^{14}N) nucleus. As a result, in this work simulations were performed with $\mathrm{D}_1^{\mathrm{k}}$ excitation in a similar manner to those previously described for simple rectangular pulses. The pulse length referred to in the next section is the total one, $t_{tot} = kt_p$, instead of only t_p when dealing with single pulses.

II.3.a Efficiency *versus* (t_{tot} & ν_1)

Fig.**6** shows a series of 2D maps that plot the on-resonance efficiency of D_1^4 trains *versus* t_{tot} and ν_1. The results observed with D_1^8 trains are shown in Fig.**S1** of the Supplementary Information. As expected, a *ca*. four times smaller rf-field is required for D_1^4 with respect to single pulse in order to efficiently excite the total spectral line-shape (compare Figs. **2** and **6**). With ν_1 = 100 kHz a very large CSA span value of Ω = 3 MHz can even be excited with t_{tot} = 2.5 μs (Fig.**6h**), whereas this value of ν_1 is ineffective when $\Omega \geq 600$ kHz when a single HP is used (Fig.**2h**: t_p = 2.5 μs).

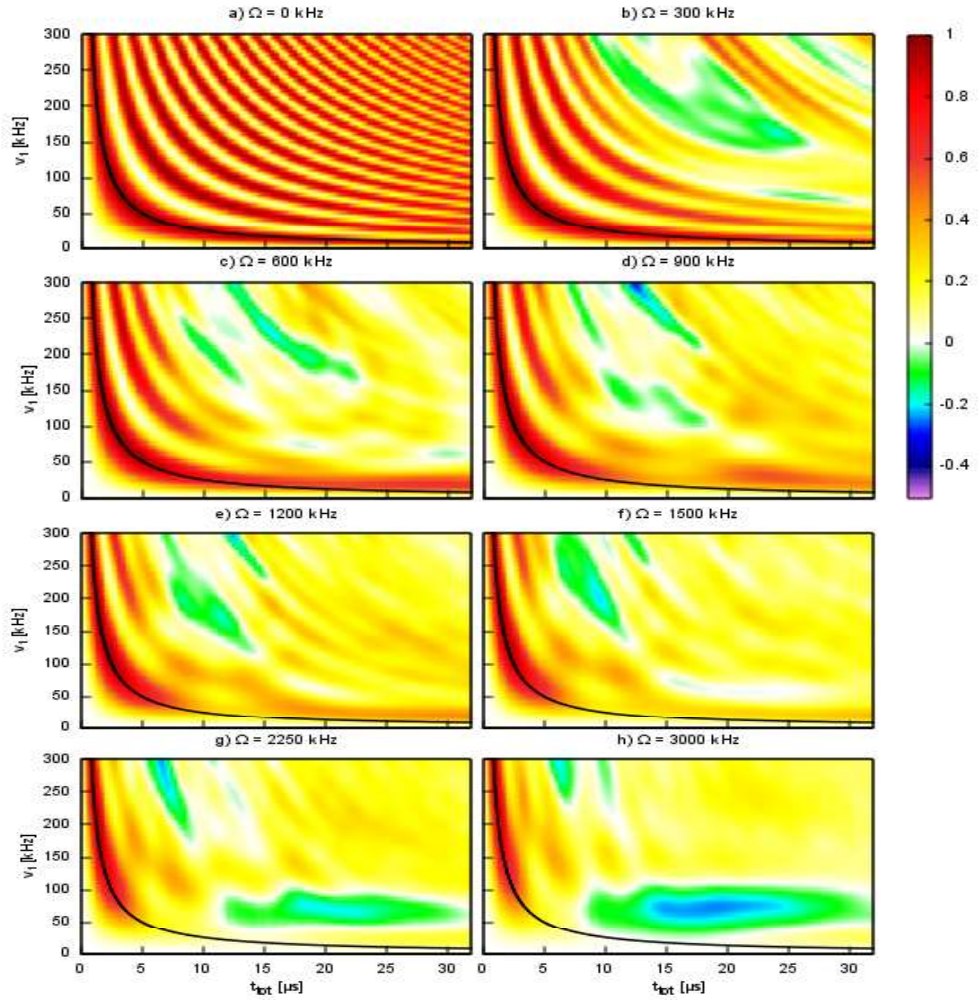

Fig.6. Simulated efficiency of ^{1}H-{^{195}Pt} *D*-HMQC experiments with $\mathbf{D}_1^4$ excitation *versus* the rf-field strength and the total pulse duration ($t_{tot} = 4t_p$), for eight CSA values, as indicated. On each sub-figure, the black curve represents the behavior for two π/2-HPs.

II.3.b Efficiency *versus* (offset & Ω)

Analysis of the efficiency of ^{1}H-{^{195}Pt} *D*-HMQC *versus* ^{195}Pt offset and CSA was carried out for D_1^4 excitation in a similar way to that which was described in section II.2.d. We have simulated two different cases with (ν_1(kHz), t_p(ns)) = (200, 310) or (100, 620), and the results are shown for eight span values in Fig.**7a** and **b**, respectively. In this case, due to the expected narrow width of each rf-spikelet (Eq.1: S_{FWHM}), for each given CSA a series of 1D excitation profiles were calculated with a very small frequency increment of 1 kHz, instead of full 2D maps. As expected, the overall envelope excitation profiles are extremely broad and for Ω = 0 they reveal that it is in fact possible to uniformly (*i.e.*, 90% of the maximum spikelet intensity) excite signals in the range of *ca*. ±1.1 MHz with D_1^4 and $t_{tot} = 4t_p$ = 1.25 µs, in agreement with E_{FWHM} = 3.75 MHz (Eq.1). This broad envelope excitation profile means that DANTE trains are well-suited to measure very large CSA values. The only limitation of these trains is the need for a limited difference of chemical shifts of the various species, ***modulo*** ν_R. Indeed, according to Eq.1 the rf-spikelets are narrow, S_{FWHM} = 18 kHz, and they are spaced every ν_R = 62.5 kHz (see the zooms in Fig.**7c**,**d**). As example, this means that two species with isotropic chemical shift frequencies separated by $\Delta\nu_{cs}$ = 58.2 kHz, see Section V, can be well excited simultaneously because $|\nu_R - \Delta\nu_{cs}|$ = 4.3 kHz, which is much smaller than S_{FWHM}. This also means that for an unknown sample, a 1D optimization of the ^{195}Pt carrier frequency is required.

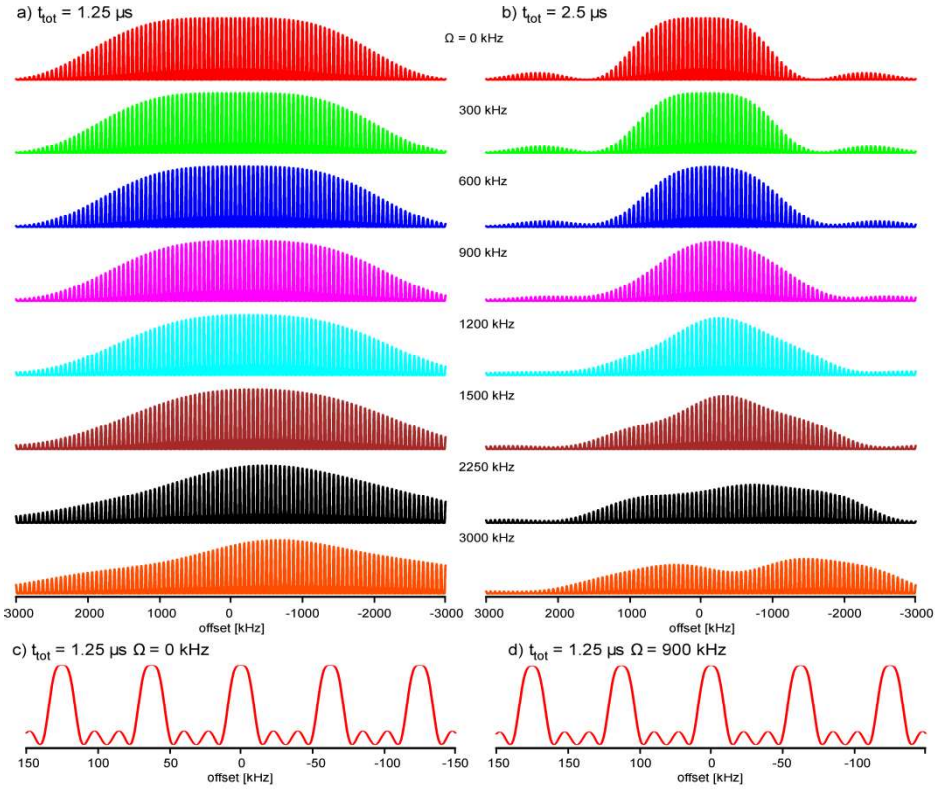

Fig.7. Simulated envelope efficiency of ^{1}H-{^{195}Pt} *D*-HMQC experiments with D_1^4 excitation with (ν_1 (kHz), t_{tot} (µs)) = (200, 1.25) (a) or (100, 2.5) (b), *versus* ^{195}Pt offset for 8 CSA span values ranging from Ω = 0-3000 kHz. (c,d) Expansions showing the individual rf-spikelets, which are CSA and rf independent (Eq.1).

II.4. Analysis of the rotor-synchronized methods versus the magnetic field

After the previous detailed information maps presented in Sections II.2 and 3, it is desirable to present in this Section the same results, but in a simpler way, which should allow the reader to make an easy choice of the excitation scheme to be used according to the magnetic field and MAS probe. For this purpose, we show in Fig.**8** the on-resonance build-up curves calculated with either SP (a-d) or D_1^4 (e-h) excitation schemes, with five CSA spans: Ω = 0, 600, 900, 1500, 3000 kHz and four rf-fields: ν_1 = 200, 150, 100, 50/42 kHz. For the weaker rf-field, 42 kHz was used for SP to stay consistent with previous simulations, but due to the broadness of the SLP region the results are similar with ν_1 = 42 and 50 kHz (Fig.**4c**,**d**).

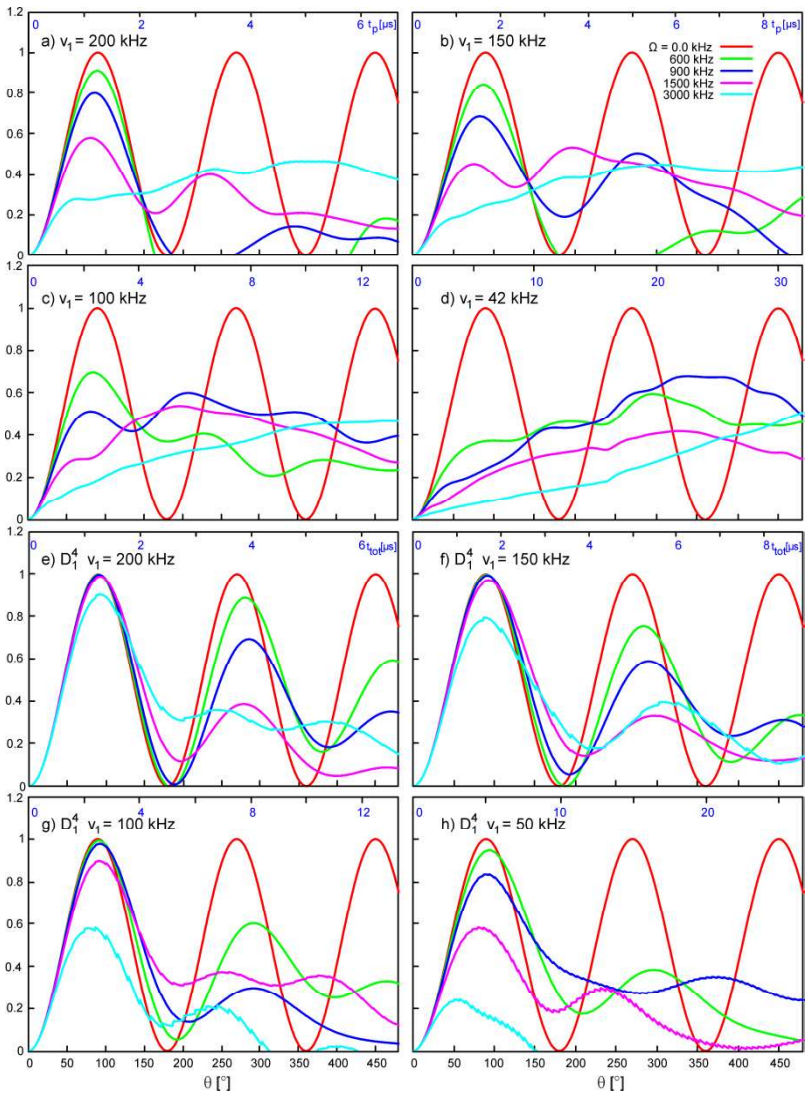

Fig.8. Simulated on-resonance build-up curves calculated with either SP (a-d) or D_1^4 (e-h) excitation schemes, with five CSA spans: Ω = 0, 600, 900, 1500, 3000 kHz, and four rf-fields: ν_1 = 200, 150, 100, 50/42 kHz, as indicated on the Figures. There are some slightly negative values (not shown) for Ω = 600 and 900 kHz in (a,b) and 3000 kHz in (g,h). The horizontal scale is shown versus the total flip angle $\theta = 2\pi\nu_1 t_p$ (a-d) or $8\pi\nu_1 t_p$ (e-h). On top of each sub-figure we show the total pulse length of each excitation scheme: t_p (a-d) or $4t_p$ (e-h).

The HP excitation is efficient if the rf-field is sufficient (e.g. $\nu_1 \geq 150$ kHz) and the CSA is small or moderate ($\Omega \leq 900$ kHz) (Fig.**8a**,**b**), which means for $B_0 \leq 14.1$ T in the case of ^{195}Pt in

cisplatin. One limitation of the HP is its sensitivity to rf-field inhomogeneity, which means that not all of the full rotor may provide a maximal signal.

The intermediate regime is useful in the case of moderate rf-field and CSAs, as observable in Fig.**8c** for the purple and dark-blue curves, with Ω = 1500 and 900 kHz, respectively.

The SLP excitation is efficient in two cases: either with low-γ nuclei (e.g. ^{57}Fe, ^{103}Rh, ^{107,109}Ag, ^{183}W) for which probes can only deliver low/moderate rf-fields, or with very high-magnetic fields where the CSA is very large (Fig.**8d**). As example, the ^{195}Pt span of cisplatin is equal to *ca*. 1.5, 2.25 and 2.8 MHz at 18.8, 28.2 and 35.2 T, respectively. A 1D optimization of the carrier frequency is recommended (Fig.**12a**,**b**).

The DANTE excitation allows for extension of the range of the hard-pulse excitation by delivering a very high effective rf-field. This means that on-resonance, it can excite a very large range of CSAs, from low to large (Fig.**8e**-**h**). Its main limitation is the fact that the carrier frequency must be optimized to excite all different species simultaneously (Fig.**12c**,**d**).

III. Simulations of constant-time *D*-HMQC 2D spectra

The previous ^{1}H-{^{195}Pt} *D*-HMQC 1D simulations shown in Figs.**2**-**8** describe the total ^{1}H signal observed with rotor-synchronized 2D experiments. However, they do not describe the detailed behavior of this signal with respect to the ^{195}Pt CSA spinning sidebands. To analyze this point, several 2D spectra were simulated with the constant-time *D*-HMQC version described by Rossini *et al*.[23] In Fig.**9** we show the ^{195}Pt projections observed when applying on the ^{195}Pt channel either two: (a) Dirac π/2-pulses; (b) D_1^4 trains or (c) HPs with ν_1 = 200 kHz; or (d) SLPs with ν_1 = 42 kHz. The effective rf-field of D_1^4 trains is so high (800 kHz) that there is no noticeable difference in between spectra shown in Fig.**9a** and **b**. This is not the case with HPs, as shown in Fig.**9c**, where sidebands are more and more attenuated when their offset increases. Contrary to the previous cases, with SLP only the sideband on-resonance with the carrier frequency, with two minor lateral bands, are excited, as shown in Fig.**9d**. However, the intensity of the on-resonance sideband is much larger than those observed in Fig.**9a**-**c**. Moreover, it is important to note that the amplitude of this resonance is quasi-independent on the carrier frequency as long as it matches one of the spinning sidebands (Fig.**9d**).

It must be noted that in spite of the fact the CSA is *ca*. 750 times larger than the dipolar interaction ($\Omega \approx$ 1.5 MHz and $D_{^{1}H\text{-}^{195}Pt} \approx$ -2 kHz), the sideband pattern largely depends on the relative interaction between the two interactions (Fig.**S2**).

It must be reminded that when recording rotor-synchronized 2D experiments, all these sidebands are folded back onto the one which is situated within the restricted spectral width of $\pm\nu_R/2$ about the carrier frequency.

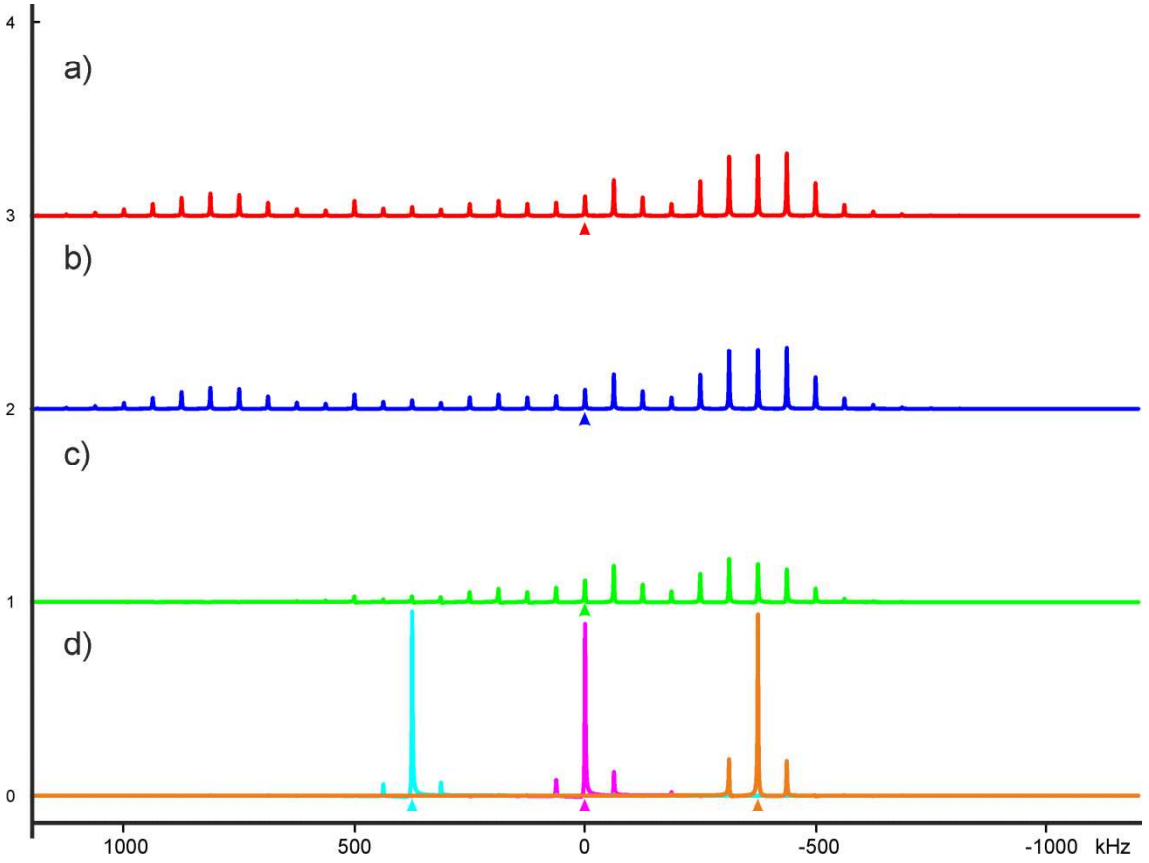

Fig.9. Simulated ^{195}Pt projection of constant-time ($2nT_R$ = 672 μs) [23] ^{1}H-{^{195}Pt} *D*-HMQC 2D spectra with on-resonance ^{195}Pt irradiation at 0 ppm with B_0 = 18.8 T, $D_{1H\text{-}195Pt}$ = -2 kHz and Ω = 1.47 MHz. (a) Dirac π/2-pulses; (b) D_1^4 trains or (c) HPs with ν_1 = 200 kHz and t = t_{tot} = 1.25 μs; and (d) SLP with ν_1 = 42 kHz and t = 24 μs. In (d), the projections observed with SLP excitation at $\pm 6\nu_R$ are also shown. In spite of the fact that the sideband situated at $6\nu_R$ in (a_j is much smaller than that at $-6\nu_R$, the two SLP signals are nearly identical. The position of the carrier frequency is indicated with a small triangle.

IV. Experimental 1D analysis of rotor-synchronized experiments

The simulations described above provide insights into the feasibility of ^{1}H-{^{195}Pt} *D*-HMQC experiments, and they allow for detailed analyses of effects that are not easily accessible experimentally, such as those related to CSA. However, they do not take into account (i) transverse relaxation phenomena which may severely decrease the signal when the indirect excitation durations are long (e.g. SLP or D_1^k), and (ii) experimental parameters such as rf-field inhomogeneity, pulse amplitude and phase transients, probe quality factors, *etc*. In order to facilitate a full and comprehensive analysis, a series of rotor-synchronized 1D experiments with t_1 = 32, 64 or 128 μs for SP, D_1^4 or D_1^8, respectively, were performed at 18.8 T with ν_R = 62.5 kHz, on the well-characterized cisplatin pharmaceutical compound which presents a single ^{195}Pt species. Unfortunately, the same experiments could not be performed at lower magnetic fields because we do not have ultra-fast MAS probes at these fields. Cisplatin has been one of the first platinum based drugs to be widely used in chemotherapy. It has recently been characterized in detail by solid-state ^{195}Pt NMR by Schurko *et al*. [44] and Rossini.[23,24] According to data provided by Rossini *et al*. and recorded at 9.4 T with ν_R = 50

kHz [23], $T_{1,1H} \approx 12$ s and the chemical shift tensor parameters of the ^{195}Pt species are: δ_{iso} = -1834 ppm with respect to K_2PtCl_6 in D_2O, and Ω = 8561 (δ_{11} = 3816, δ_{22} = -4573, δ_{33} = -4745) ppm, which corresponds to Ω = 1.47 MHz at B_0 = 18.8 T. It must be noted that the present experimental value of δ_{iso} = -1828 ppm is slightly different because the spinning speed was higher, ν_R = 62.5 kHz, and hence also the temperature of the sample.

IV.1. Efficiency *versus* (t_{tot} & ν_1)

The first part of the discussion focusses on the on-resonance build-up curves obtained for experiments performed with single pulses (SP) or D_1^k DANTE trains (Fig.10). On each figure, a dashed red line indicates the maximum intensity observed in (e), and also the relative maximum value.

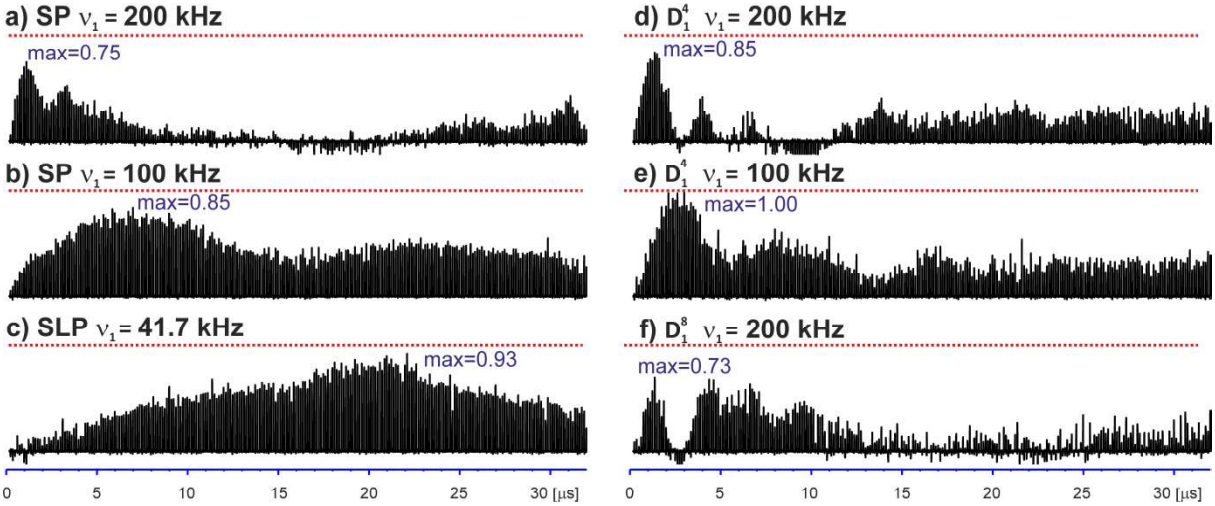

Fig.10. Experimental cisplatin ^{1}H-{^{195}Pt} rotor-synchronized *D*-HMQC on-resonance 1D ^{1}H signal with τ_{RD} = 13 s and NS = 16, *versus* the pulse length on ^{195}Pt: t_p (SP) or $t_{tot} = kt_p$ (D_1^k), with ν_1 = 200 (a,d,f), 100 (b,e), 42 kHz (c).

With ν_1 = 200 kHz (Fig.10a), the first two maxima of the ^{1}H signal correspond to HPs with $\theta = \pi/2$ or $3\pi/2$ with $t_p \approx 1.25$ and 3.7 µs, respectively, and the second maximum is smaller than the first one, as shown in Figs.4a and 8a. In this case, no other efficient excitation regime is observed. With ν_1 = 100 kHz (Fig.10b), no HP excitation is observed, and the first maximum, which is observed for $t_p \approx$ 5-6 µs, corresponds to the intermediate regime, whereas the second one with $t_p \approx$ 20-25 µs is the beginning of the broad SLP excitation profile. This description is in good agreement with the simulations shown in Figs.4b and 8b. When ν_1 = 42 kHz = $2\nu_R/3$, only the SLP excitation regime is visible at $t_p \approx$ 20-22 µs, which is close to $1.5T_R$, in agreement with Fig.4c and 8d. Despite the relatively low rf-field used, it can be seen that SLP is the most efficient regime with SP excitation.

With DANTE excitation (Fig.10d-f), the SLP and intermediate regimes are inefficient, and only the HP regime is visible, as shown in Fig.8e-h. With D_1^4 trains and ν_1 = 100 or 200 kHz, it leads to the two maxima observed at $t_{tot} \approx$ 2.5 and 7 or 1.25 and 3.7 µs, respectively. As shown in the simulations presented above (Figs.7g,h and 8e-h), with D_1^4 pulses for each rf-value the second maximum is less efficient than the first one (Fig.10d,e). With D_1^8 pulse and ν_1 = 200 kHz, the intensity of the maximum signal observed with $t_{tot} \approx$ 1.25 µs is decreased with respect to

that observed for D_1^4 train (compare Fig.**10d** and **f**). This decrease is likely to be related to two effects. The first effect corresponds to the losses that occur during $8T_R$, instead of only $4T_R$ for D_1^4 pulses. The second one is related to the increased amount of transients. Indeed, with respect to D_1^4, there are twice as many pulses and the importance of such transients increases with such short pulses of $t_p = t_{tot}/8 \approx 155$ ns. This transient-related attenuation is much smaller for the second maximum due to the fact that the t_p value is *ca*. 3 times longer. These transient-related effects are certainly also the reason why the 1st maximum observed in (d) is smaller than in (e). Globally, the amplitude of the maximum efficiency observed with D_1^4 and ν_1 = 100 kHz is similar to that observed with SLP, but with a *ca*. 2.5 times larger rf-field strength (compare Fig.**10c** and **e**).

IV.2 Efficiency *versus* (offset & ν_1)

The second factor that will be discussed is the robustness to offset. This is a very important point in the case of nuclei with a very broad isotropic chemical shift range; *e.g.*, 13,000 ppm for ^{195}Pt [16]. Fig.**11** shows the ^{1}H-{^{195}Pt} 1D ^{1}H signal from cisplatin *versus* ^{195}Pt offset over ±1 MHz, for excitation with two HPs (Fig.**11a**,**b**), two SLPs (Fig.**11c**) or two D_1^4 trains (Fig.**11d**). In the first HP cases, the offset width is equal to FWHM $\approx 5\nu_1$ (Fig.**11a**,**b**). In the last D_1^4 case (Fig.**11d**), the excitation pattern is composed of a comb of rf-spikelets, separated by multiples of ν_R from the carrier frequency at 0 ppm. Following Eq.1, the width for the envelope of these spikelets is $E_{FWHM} \approx 1.1/t_p = 1.1k/t_{tot} \approx 4.5k\nu_1$, and each of these spikelets has a width of $S_{FWHM} \approx \nu_R/k$. The offset profile of SLP (Fig.**11c**) is a compromise in between those of Figs.**11a**,**b** and **11d**. It is also composed of a comb of spikelets every ν_R, but each of them is much broader than in Fig.**11d**, which thus provides a much higher level of robustness. Moreover, it has already been shown that the widths of the spikelets and of their envelope increase with ν_R due to its proportionality to the optimum rf-value: $\nu_1 \approx 2\nu_R/3$. [30]

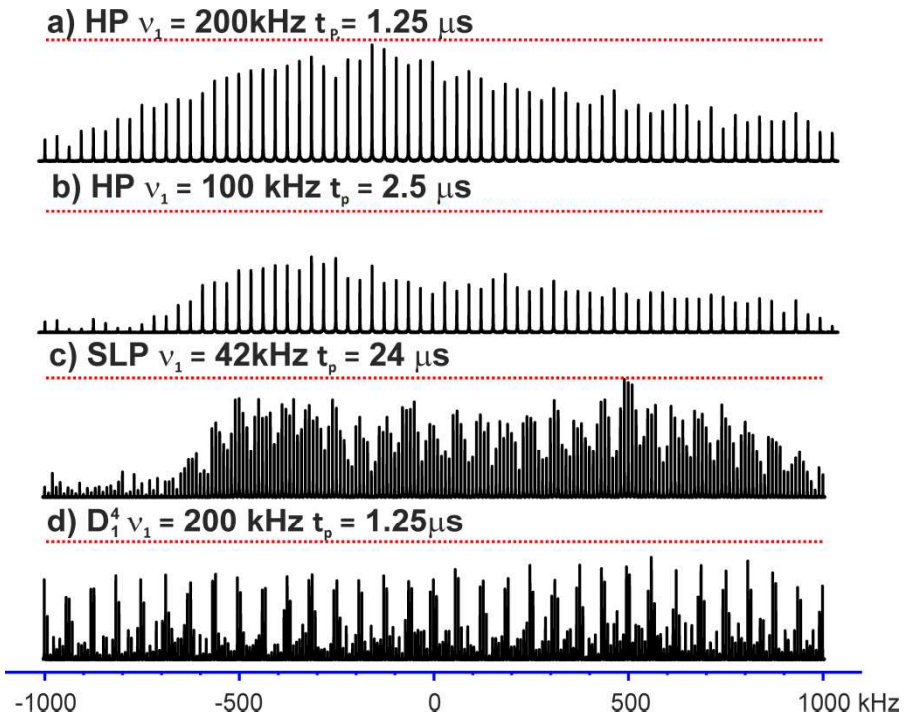

Fig.11. Experimental cisplatin ^{1}H-{^{195}Pt} rotor-synchronized *D*-HMQC ^{1}H signal with τ_{RD} = 13 s and NS = 16 *versus* the ^{195}Pt offset, with various types of excitation, rf-field and pulse length (t_p or t_{tot}) as indicated on the subfigures. The offset step is equal to $\nu_R/2$ = 31.25 (a,b), 10 (c) and 8 kHz (d). It must be noted that in (b) the pulse length does not correspond to the optimum intermediate regime (Fig.**10b**).

V. Experimental analysis of ^{1}H-{^{195}Pt} 2D experiments

Secondly, an attempt was made to verify the previous simulations, shown in Fig.**7c**,**d**, which describe the behavior of the signal with respect to the ^{195}Pt offset. Cis- and transplatin were used as test samples because they are well characterized [23,24,44]. The NMR parameters of the single ^{195}Pt species of transplatin, observed at 9.4 T with ν_R = 50 kHz, are $T_{1,1H}$ = 17 s, δ_{iso} = -2181 and Ω = 9100 ppm, which corresponds to Ω = 1565 kHz at 18.8 T [23]. At 18.8 T and ν_R = 62.5 kHz, we observed δ_{iso} = -2167 ppm and $T_{1,1H}$ = 13 s. This means that, when observed with ν_R = 62.5 kHz, cis- and transplatin isotropic chemical shifts are separated at by $\Delta\nu_{iso}$ = 339 ppm = 58.2 kHz at 18.8 T. Both samples present a single amine ^{1}H resonance at the same position (δ_{iso} = 4.25 ppm), and hence in the following only the ^{195}Pt projections of the 2D spectra are shown. It must be remembered that with such large CSA, the t_1 noise may be important for rotor-synchronized 2D experiments. This noise was indeed large with a recycling delay of τ_{RD} = 13 s, as used in Figs.**10** and 11, but it decreased greatly with the much shorter value of τ_{RD} = 1 s, as very recently recommended by Perras and Pruski. [45]

V.1. Rotor-synchronized 2D experiments

Figs.**12a**,**b** show the ^{195}Pt projections of 2D rotor-synchronized ^{1}H-{^{195}Pt} spectra of a mechanical mixture of cis- and transplatin recorded with SLP and 6 different carrier frequencies every 10.3 kHz. Figs.**12c**,**d** show those of a pure sample of cisplatin recorded with D_1^4 *versus* the ^{195}Pt carrier frequency with 5 kHz step.

As expected, the signal is maximum for on-resonance irradiation, and it can be observed that the robustness to offset is much larger with SLP compared to D_1^4, as previously shown (Fig.**7**

and 11). It is important to note that the position of the ^{195}Pt carrier frequency can easily be optimized with 1D experiments (not shown).

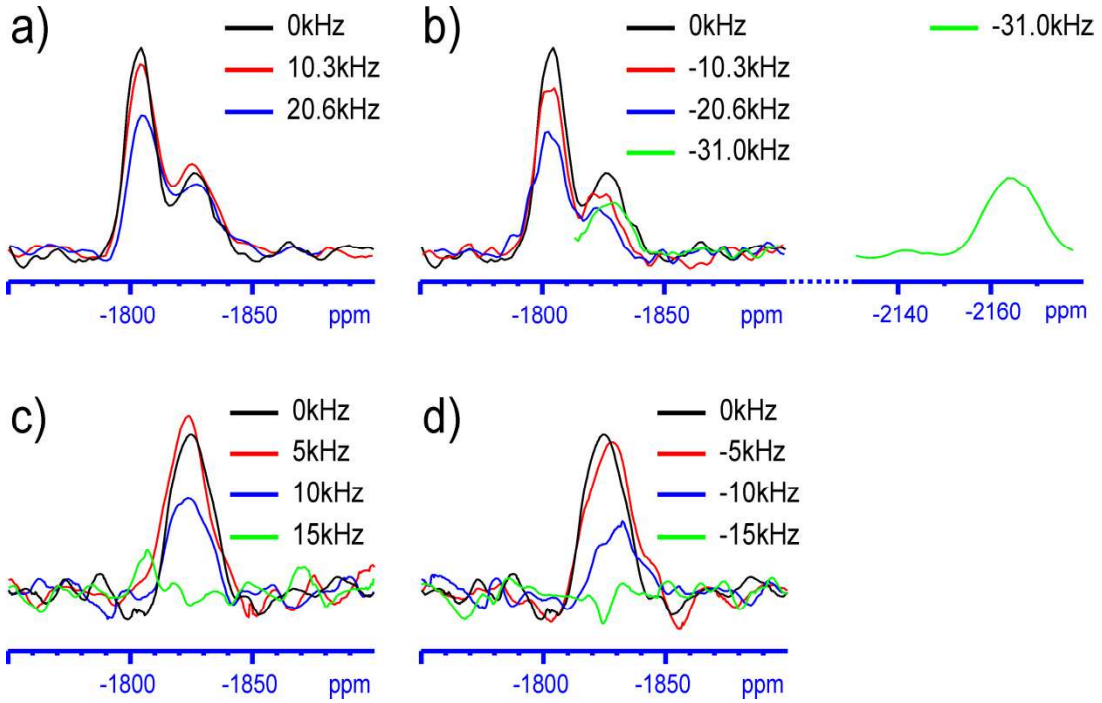

Fig.12. Experimental ^{195}Pt projections of ^{1}H-{^{195}Pt} rotor-synchronized *D*-HMQC 2D spectra recorded at 18.8 T with ν_R = 62.5 kHz, τ_{RD} = 1 s, 64 complex t_1 points, NS = 64, and T_{exp} =2.5 hrs, *versus* the position of the ^{195}Pt carrier frequency. (a,b) SLP excitation (ν_1 = 42 kHz, t_p = 24 μs) of a cis- and transplatin mixture with ν_{offset} = 0, ±10.33, ±20.66, -31 kHz. (c,d) D_1^4 excitation (ν_1 = 200 kHz, t_{tot} = 1.25 μs) of cisplatin with ν_{offset} = 0, ±5, ±10, ±15 kHz. The carrier frequency is defined with respect to: (a,b) the middle of the two signals (-1817 ppm), (c,d) the on resonance signal (-1828 ppm).

In Fig.12b one observes that for ν_{offset} = -31 kHz, the resonance of transplatin is shifted by ν_R with respect to its position observed for the other offset values. This shift is related to the fact the spectral width is limited to $\pm\nu_R/2$ = ±31.25 kHz with respect to the carrier frequency, and hence all spinning sidebands related to transplatin then fold-back onto another sideband. This means that it is impossible to determine the actual isotropic chemical shift from one rotor-synchronized spectra (e.g. Fig.12a,b). Moreover, with one non-rotor-synchronized constant-time *D*-HMQC experiment, or even with one single-pulse experiment, it is very difficult to determine the actual chemical shift by simulating the comb of experimental sidebands, as will be shown in Section V.2. Practically, this limitation occurs for all experiments, except with the aMAT-D-HMQC sequence [24]. However, this sequence requires a very large indirect spectral width and 7 pulses on the indirect channel, which lead to long experimental times. Acquiring two 2D spectra, rotor-synchronized to minimize the experimental time, with two different spinning speeds, may be simpler and more efficient. As already mentioned, the HP and SLP excitations are complementary in the sense that they mainly excite small/moderate and moderate/large CSAs, respectively, as observed for ^{195}Pt (IV) and (II), respectively. Therefore, with an unknown sample, two spectra with HP and SLP excitations, could be acquired with two different spinning speeds to simultaneously determine the "true" chemical shifts and efficiently excite all resonances. The determination of the "true" chemical shifts is demonstrated in Fig.13 on the mechanical mixture of cis- and transplatin. In this case, only SLP excitation was used because both compounds have similar large CSA values. Indeed, when

increasing the spinning speed from ν_R = 62.5 to 64.1 kHz, it can be observed that the resonances at -1828 and -2167 ppm do not move, meaning that they correspond to the isotropic chemical shifts of cis- and transplatin, respectively, whereas the two other resonances are shifted by 1.6 kHz, which means that they correspond to first sidebands.

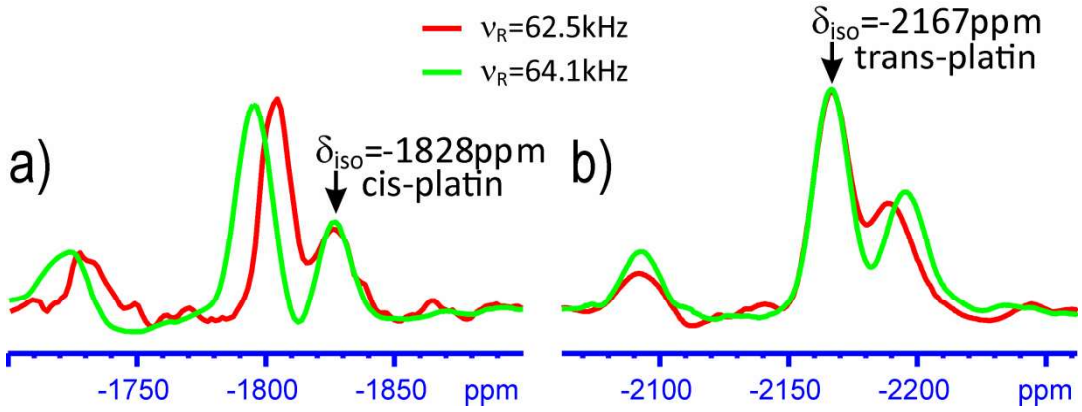

Fig.13. Experimental ^{195}Pt projection of a mixture of cis- and transplatin ^{1}H-{^{195}Pt} rotor-synchronized *D*-HMQC 2D spectra recorded with SLP (ν_1 = 42 kHz, t_p = 24 µs) at 18.8 T with ν_R = 62.5 and 64.1 kHz, τ_{RD} = 0.8 s, 64 t_1-complex points and NS = 32, T_{exp} = 1 hr. The ^{195}Pt carrier frequency is situated in the middle of the two resonances.

V.2. Constant-time 2D experiments

Attempts were also made to verify the previous simulations, shown in Fig.**9**, which describe the detailed behavior of the signal with respect to the ^{195}Pt CSA spinning sidebands. For this purpose, several ^{1}H-{^{195}Pt} 2D spectra of cisplatin were recorded with constant time acquisition, as proposed by Rossini *et al*. [23] (Fig.**14**). Indeed, the analysis of the signal along the ^{195}Pt axis may help the readers to better understand how these different sequences excite the sideband patterns. With SLP, only the sideband on-resonance with the carrier frequency, with two minor lateral ones, are excited, as shown in the simulations (compare Figs.**9d** and **14d**). With HP and D_1^4 (Fig.**14b**,**c**), the S/N is much lower than with SLP because the signal is distributed among many sidebands. With HP, the external sidebands are quite attenuated, as already shown with the simulations (Fig.**9b**). This is less the case with D_1^4, which scales up by four the effective rf-field (Fig.**9c**). The 2D constant-time experiments with HP and D_1^4 excitations have been recorded several times each (not shown) with the same sample, same spinning speed and same rotor, and we have observed that, due to spectrometer instabilities, the sideband patterns were never the same for a given experiment. Therefore, considering: (i) the line-shape distortions related to limited rf-field and spectrometer instability, and the required knowledge of (ii) the $D_{1H\text{-}195Pt}$ value and of (iii) its relative orientation with respect to the CSA tensor (Fig.**S2**), determining the isotropic chemical shift by fitting the sideband comb seems hazardous. Moreover, it must be reminded that the integrated sideband intensities, not their amplitudes, should be taken into account when fitting the experimental data. Indeed, due to spinning speed fluctuations, the external sidebands are more broadened, and hence attenuated, than those close to the carrier frequency. This broadening may be important in the case of large CSAs and poorly stabilized spinning speeds.

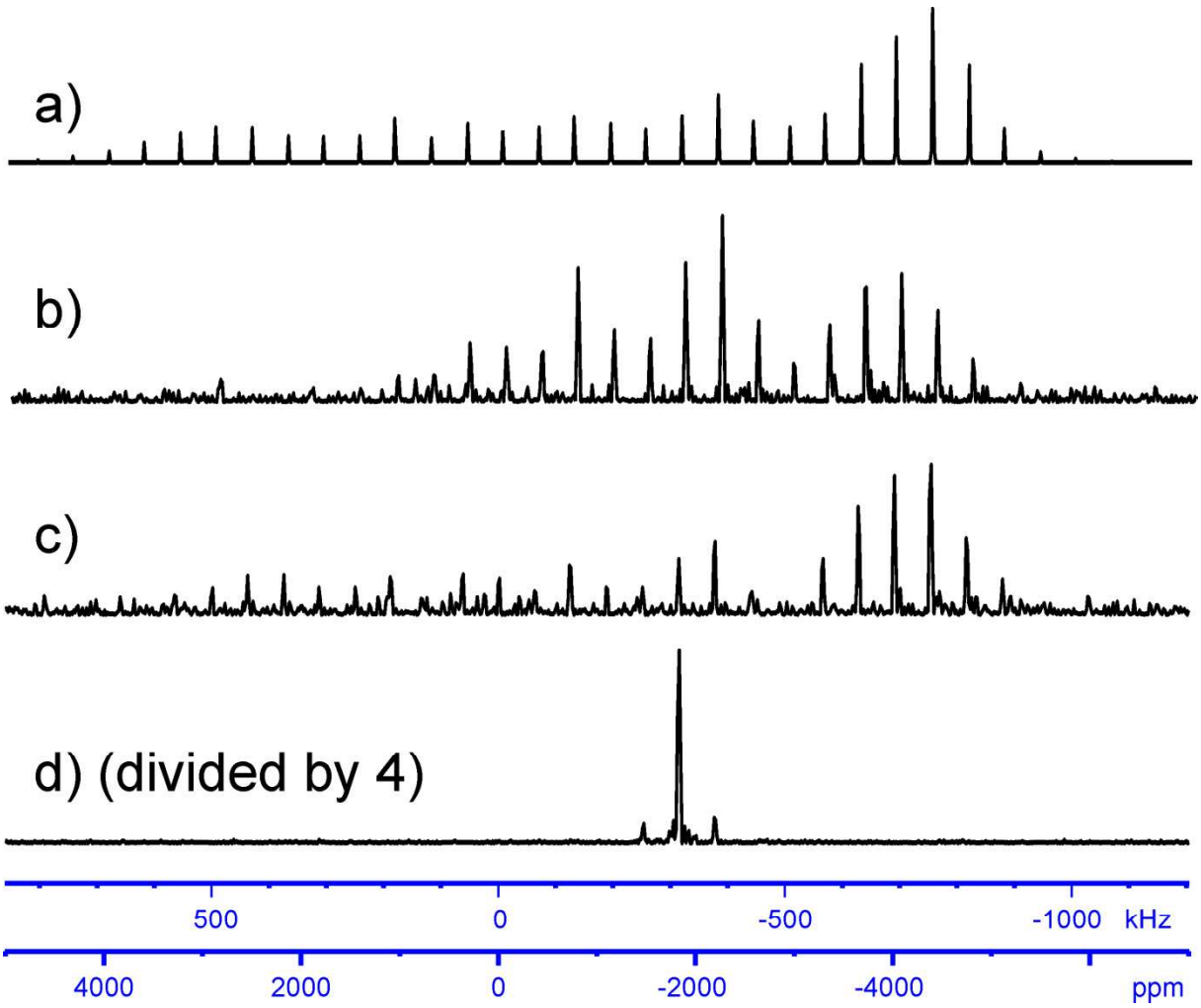

Fig.14. Cisplatin MAS spectra at 18.8 T with ν_R = 62.5 kHz. (a) 1D spectrum simulated after a Dirac single pulse. (b-d) projections onto the ^{195}Pt axis of ^{1}H-{^{195}Pt} *D*-HMQC 2D constant-time spectra ($2nT_R$ = 0.176ms [23]) with ^{195}Pt on-resonance excitation, recorded with $SR4_1^2$: m = 32, τ_{RD} = 0.8 s, NS = 64, 512 complex t_1 points, Δt_1 = 0.4 µs (SW1 = 2.5 MHz), T_{exp} = 13h h. ^{195}Pt excitation with (ν_1 (kHz), t_p/t_{tot} (µs)) = (200, 1.25) HP (b) or D_1^4 (c) or (42, 24) SLP (d).

VI. Conclusions

This work has provided extended insights into possible applications of the ^{1}H-{X} *D*-HMQC sequence in studies involving spin-1/2 nuclei subject to very large anisotropic interactions, such as ^{195}Pt. The analysis was carried out at a spinning speed of ν_R = 62.5 kHz, using three different excitation schemes: Hard Pulse (HP), Selective Long Pulse (SLP) or DANTE trains. This study used SIMPSON simulations and several experiments performed at B_0 = 18.8 T either in 1D mode on cisplatin, to compare the efficiency of these three excitation schemes, or with 2D spectra on cisplatin or mixtures of cis- and transplatin.

The HP excitation is efficient if the rf-field provided by the probe is sufficient (e.g. $\nu_1 \geq 150$ kHz) with small or moderate CSAs ($\Omega \leq 1000$ kHz) (Fig.**8a**,**b**). One possible limitation of HP is its sensitivity to rf-field, which means that not all the full rotor sample may provide a large signal.

The SLP excitation ($\nu_1 \approx 2\nu_R/3$ and $t_p \approx 1.5T_R$) is mostly efficient with high-magnetic fields where the CSA can be very large (Fig.**8d**). This scheme is very robust with respect to rf-power and pulse duration. The relatively high efficiency of SLP comes from the fact that all crystallites in the rotor provide a signal when their CSA interaction frequency matches the excitation due to sample rotation. This also means that this signal is always at the carrier frequency, and not at the isotropic chemical shift.

The intermediate regime between HP and SLP, is useful in the case of moderate rf-field and CSAs, as observable in Fig.**8c**.

The DANTE excitation allows extending the range of the hard-pulse excitation by delivering a very high effective rf-field. This means that it can excite a very wide range of CSAs, from low to large (Fig.**8e**-**h**). Its main limitation is the fact that the carrier frequency must be optimized to excite efficiently all different species simultaneously. However, this optimization can be done in a 1D way, and hence is not time consuming.

It must be mentioned that, except for the aMAT-HMQC method [24], in all types of HMQC experiments dealing with very large CSA, rotor-synchronized or not, it is necessary to collect two 2D spectra with different spinning speeds in order to discriminate the isotropic lines from the spinning sidebands. This can be done by recording two 2D spectra with two different spinning speeds either with two DANTE train acquisitions or by combining two complementary spectra one with HP and the other with SLP excitations.

VII. Simulation and experimental methods

Solid-state NMR experiments were performed at B_0 = 18.8 T using a standard bore Bruker magnet with an AV-IV spectrometer console. The samples were packed into a 1.3 mm rotor and used in a ^{1}H/BB (^{31}P-^{14}N) CPMAS probe operating at ^{1}H and ^{195}Pt resonance frequencies of 800.1 and 171.7 MHz, respectively. The spinning speed was controlled by a Bruker MAS-III unit and was set to ν_R = 62.5 kHz (T_R = 16 µs), except in Fig.**13**: ν_R = 64.1 kHz. The MAS rate stability was estimated using an oscilloscope to be ±15 Hz. For this experiment, a high spinning speed stability is mandatory due to the large number of sidebands. The optimization of ^{1}H $\pi/2$ and π pulses, as well as of $\mathrm{SR4}_1^2$ recoupling, was directly done on the samples. The ^{1}H rf-field was set to 208 kHz for $\pi/2$ and π pulses and optimized to 162 kHz during $\mathrm{SR4}_1^2$. The discrepancy between the experimental rf-optimum and the theoretical values (125 kHz) for $\mathrm{SR4}_1^2$ is likely to be caused by rf-field inhomogeneity and strong ^{1}H-^{1}H dipolar interactions. The ^{195}Pt rf-pulse lengths and amplitudes were calibrated indirectly using the ^{127}I resonance of KI, as proposed by Rossini *et al.*[23]

Simulations were performed with ν_R = 62.5 kHz and the SIMPSON version 4.0.0c [46,47]. Powder averaging was performed with 5291 $\{\alpha_{MR}, \beta_{MR}, \gamma_{MR}\}$ Euler angles that described the orientation of the molecule in the rotor frame. The 143 $\{\alpha_{MR}, \beta_{MR}\}$ pairs were selected according to the ZCW method,[48,49,50] whereas the 37 γ_{MR} angles were regularly stepped from 0 to 360°. The spin system was one isolated ^{195}Pt-^{1}H spin pair with an interatomic distance of 2.34 Å, leading to a dipolar coupling value of $D_{^{1}H\text{-}^{195}Pt}$ = -2 kHz. The two ^{1}H $\pi/2$ and π pulses were set to be perfect Dirac ones. Two examples of SIMPSON input files are provided

in the Supporting Information. In all cases, the CSA is described using the span value $\Omega = \delta_{11} - \delta_{33}$, according to the Herzfeld-Berger Convention.[51]

Supplementary Information. Figures S1 and S2, input files used for SIMPSON simulations, and pulse programs.

VIII. Acknowledgments

PP is grateful for funding from the MOBILITY PLUS program (grant no. 1630/MOB/V/2017/0). The computational resources were provided by the Polish Infrastructure for Supporting Computational Science in the European Research Space (PL-GRID). Institut Chevreul (FR 2638), Ministère de l'Enseignement Supérieur et de la Recherche, Région Hauts-de-France and the European Union (FEDER/ERDF) are acknowledged for supporting and partially funding this work. Financial and technical supports from the TGIR-RMN-THC FR 3050 CNRS for conducting the research are gratefully acknowledged. Authors also acknowledge contract CEFIPRA nos. 85208-E, PRC CNRS-NSFC, ANR-14-CE07-0009-01 and ANR-17-ERC2-0022 (EOS). OL acknowledges financial support from Institut Universitaire de France (IUF).

---

[1] D. Sakellariou, A. Lesage, P. Hodgkinson, L. Emsley, Homonuclear dipolar decoupling in solid-state NMR using continuous phase modulation, *Chem. Phys. Lett.* 319 (**2000**) 253–260. doi:10.1016/S0009-2614(00)00127-5.

[2] E. Vinogradov, P.K. Madhu, S. Vega, High-resolution proton solid-state NMR spectroscopy by phase-modulated Lee-Goldburg experiment, *Chem. Phys. Lett.* 314 (**1999**) 443–450. doi:10.1016/S0009-2614(99)01174-4.

[3] R. Zhang, K.H. Mroue, A. Ramamoorthy, Proton-based ultrafast Magic Angle Spinning Solid-State NMR spectroscopy, *Acc. Chem. Res.* 50 (**2017**) 1105–1113. doi:10.1021/acs.accounts.7b00082.

[4] K. Mao, J.W. Wiench, V.S.-Y. Lin, M. Pruski, Indirectly detected through-bond chemical shift correlation NMR spectroscopy in solids under fast MAS: Studies of organic–inorganic hybrid materials, *J. Magn. Reson.* 196 (**2009**) 92–95. doi:10.1016/j.jmr.2008.10.010.

[5] K. Mao, M. Pruski, Directly and indirectly detected through-bond heteronuclear correlation solid-state NMR spectroscopy under fast MAS, *J. Magn. Reson.* 201 (**2009**) 165–174. doi:10.1016/j.jmr.2009.09.004.

[6] T. Kobayashi, K. Mao, P. Paluch, A. Nowak-Król, J. Sniechowska, Y. Nishiyama, D.T. Gryko, M.J. Potrzebowski, M. Pruski, Study of intermolecular interactions in the corrole matrix by Solid-State NMR under 100 kHz MAS and theoretical calculations, *Angew. Chem. Int. Ed.* 52 (**2013**) 14108–14111. doi:10.1002/anie.201305475.

[7] Y. Hong, T. Asakura, Y. Nishiyama, 3D $^{14}N/^{1}H$ DQ/^{1}H SQ Correlation Solid-State NMR for probing the parallel and anti-parallel Beta-sheet arrangement of oligo-peptides at natural abundance, *ChemPhysChem.* 19 (**2018**) 1841–1845. doi:10.1002/cphc.201800392;

[8] M.K. Pandey, J.-P. Amoureux, T. Asakura, Y. Nishiyama, Sensitivity-enhanced $^{14}N/^{14}N$ correlations to probe inter beta-sheet interactions using fast magic angle spinning solid-state NMR in biological solids, *Phys. Chem. Chem. Phys.*, 18 (**2016**) 22583-22589.

[9] N.T. Duong, S. Raran-Kurussi, Y. Nishiyama, V. Agarwal, Quantitative $^{1}H–^{1}H$ distances in protonated solids by frequency-selective recoupling at fast Magic Angle Spinning NMR, *J. Phys. Chem. Lett.* 9 (**2018**) 5948–5954. doi:10.1021/acs.jpclett.8b02189.

[10] E. Barbet-Massin, A.J. Pell, J.S. Retel, L.B. Andreas, K. Jaudzems, W.T. Franks, A.J. Nieuwkoop, M. Hiller, V. Higman, P. Guerry, A. Bertarello, M.J. Knight, M. Felletti, T. Le Marchand, S. Kotelovica, I. Akopjana, K. Tars, M. Stoppini, V. Bellotti, M. Bolognesi, S. Ricagno, J.J. Chou, R.G. Griffin, H. Oschkinat, A. Lesage, L. Emsley, T. Herrmann, G. Pintacuda, Rapid proton-detected NMR assignment for proteins with fast Magic Angle Spinning, *J. Am. Chem. Soc.* 136 (**2014**) 12489–12497. doi:10.1021/ja507382j.

[11] A. Marchanka, J. Stanek, G. Pintacuda, T. Carlomagno, Rapid access to RNA resonances by proton-detected solid-state NMR at > 100 kHz MAS, *Chem. Comm.* 54 (**2018**) 8972–8975. doi:10.1039/C8CC04437F.

[12] J. Stanek, L.B. Andreas, K. Jaudzems, D. Cala, D. Lalli, A. Bertarello, T. Schubeis, I. Akopjana, S. Kotelovica, K. Tars, A. Pica, S. Leone, D. Picone, Z.-Q. Xu, N.E. Dixon, D. Martinez, M. Berbon, N. El Mammeri, A. Noubhani, S. Saupe, B. Habenstein, A. Loquet, G. Pintacuda, NMR spectroscopic assignment of backbone and side-chain protons in fully protonated proteins: microcrystals, sedimented assemblies, and amyloid fibrils, *Angew. Chem. Int. Ed.* 55 (**2016**) 15504–15509. doi:10.1002/anie.201607084.

[13] P. Paluch, T. Pawlak, M. Oszajca, W. Lasocha, M.J. Potrzebowski, Fine refinement of solid state structure of racemic form of phospho-tyrosine employing NMR Crystallography approach, *Solid State Nucl. Magn. Reson.* 65 (**2015**) 2–11. doi:10.1016/j.ssnmr.2014.08.002.

[14] P. Paluch, T. Pawlak, K. Lawniczak, J. Trébosc, O. Lafon, J.-P. Amoureux, M.J. Potrzebowski, Simple and robust study of backbone dynamics of crystalline proteins employing ^{1}H-^{15}N dipolar coupling dispersion, *J. Phys. Chem. B.* 122 (**2018**) 8146–8156. doi:10.1021/acs.jpcb.8b04557.

[15] A.-C. Pöppler, J.-P. Demers, M. Malon, A.P. Singh, H.W. Roesky, Y. Nishiyama, A. Lange, Ultrafast Magic-Angle Spinning: benefits for the acquisition of ultra-wide-Line NMR spectra of heavy spin 1/2 nuclei, *ChemPhysChem.* 17 (**2016**) 812–816. doi:10.1002/cphc.201501136.

[16] B.M. Still, P.G.A. Kumar, J.R. Aldrich-Wright, W.S. Price, 195Pt NMR: theory and application, *Chem. Soc. Rev.* 36 (**2007**) 665–686. doi:10.1039/B606190G.

[17] L.A. O'Dell, R.W. Schurko, QCPMG using adiabatic pulses for faster acquisition of ultra-wideline NMR spectra, *Chem. Phys. Lett.* 464 (**2008**) 97–102. doi:10.1016/j.cplett.2008.08.095.

[18] K.J. Harris, A. Lupulescu, B.E.G. Lucier, L. Frydman, R.W. Schurko, Broadband adiabatic inversion pulses for cross polarization in wideline solid-state NMR spectroscopy, *J. Magn. Reson.* 224 (**2012**) 38–47. doi: 10.1016/j.jmr.2012.08.015.

[19] T. Kobayashi, F.A. Perras, T.W. Goh, T.L. Metz, W. Huang, M. Pruski, DNP-Enhanced ultra-wideline solid-state NMR spectroscopy: studies of Platinum in Metal–Organic Frameworks, *J. Phys. Chem. Lett.* 7 (**2016**) 2322–2327. doi:10.1021/acs.jpclett.6b00860.

[20] O. Pecher, D.M. Halat, J. Lee, Z. Liu, K.J. Griffith, M. Braun, C.P. Grey, Enhanced efficiency of solid-state NMR investigations of energy materials using an external automatic tuning/matching (eATM) robot, *J. Magn. Reson.* 275 (**2017**) 127–136. doi:10.1016/j.jmr.2016.12.008.

[21] M.-H. Thibault, B.E.G. Lucier, R.W. Schurko, F.-G. Fontaine, Synthesis and solid-state characterization of platinum complexes with hexadentate amino- and iminophosphine ligands, *Dalton Trans.* (**2009**) 7701. doi:10.1039/b907737e.

[22] R.W. Schurko, Ultra-wideline Solid-State NMR spectroscopy, *Acc. Chem. Res.* 46 (**2013**) 1985–1995. doi:10.1021/ar400045t.

[23] A.J. Rossini, M.P. Hanrahan, M. Thuo, Rapid acquisition of wideline MAS solid-state NMR spectra with fast MAS, proton detection, and dipolar HMQC pulse sequences, *Phys. Chem. Chem. Phys.* 18 (**2016**) 25284–25295. doi:10.1039/C6CP04279A.

[24] F.A. Perras, A. Venkatesh, M.P. Hanrahan, T.W. Goh, W. Huang, A.J. Rossini, M. Pruski, Indirect detection of infinite-speed MAS solid-state NMR spectra, *J. Magn. Reson.* 276 (2017) 95–102. doi:10.1016/j.jmr.2017. 01.010.

[25] A.S. Tatton, T.N. Pham, F.G. Vogt, D. Iuga, A.J. Edwards, S.P. Brown, Probing hydrogen bonding in cocrystals and amorphous dispersions using ^{14}N-^{1}H HMQC solid-state NMR, *Mol. Pharmaceutics*. 10 (**2013**) 999–1007. doi:10.1021/mp300423r.

[26] Z. Gan, I. Hung, Y. Nishiyama, J.-P. Amoureux, O. Lafon, H. Nagashima, J. Trébosc, B. Hu, ^{14}N overtone nuclear magnetic resonance of rotating solids, *J. Chem. Phys.* 149 (**2018**) 064201. doi:10.1063/1.5044653.

[27] E. Dib, T. Mineva, B. Alonso, Recent Advances in ^{14}N Solid-State NMR, *Ann. Rep. NMR Spectrosc.*, Elsevier, **2016**: 175–235. doi:10.1016/bs.arnmr.2015.08.002.

[28] A.G.M. Rankin, J. Trébosc, P. Paluch, O. Lafon, J.-P. Amoureux, Evaluation of excitation schemes for indirect detection of ^{14}N *via* solid-state HMQC NMR experiments. *J. Magn. Reson.* Under correction.

[29] Y. Li, J. Trébosc, B. Hu, M. Shen, J.-P. Amoureux, O. Lafon, Indirect detection of broad spectra in solid-state NMR using interleaved DANTE trains, *J. Magn. Reson.* 294 (**2018**) 101–114. doi:10.1016/j.jmr.2018.07.005.

[30] M. Shen, J. Trébosc, O. Lafon, Z. Gan, F. Pourpoint, B. Hu, Q. Chen, J.-P. Amoureux, Solid-state NMR indirect detection of nuclei experiencing large anisotropic interactions using spinning sideband-selective pulses, *Solid State Nucl. Magn. Reson.* 72 (**2015**) 104–117. doi:10.1016/j.ssnmr.2015.09.003.

[31] H. Nagashima, A.S. Lilly Thankamony, J. Trébosc, L. Montagne, G. Kerven, J.-P. Amoureux, O. Lafon, Observation of proximities between spin 1/2 and quadrupolar nuclei in solids: Improved robustness to chemical shielding using adiabatic symmetry-based recoupling, *Solid State Nucl. Magn. Reson.* 94 (**2018**) 7–19. doi:10.1016/j.ssnmr.2018.07.001.

[32] X. Lu, O. Lafon, J. Trébosc, G. Tricot, L. Delevoye, F. Mear, L. Montagne, J.-P. Amoureux, Observation of proximities between spin-1/2 and quadrupolar nuclei: which hetero-nuclear dipolar recoupling method is preferable?, *J. Chem. Phys*, 137 (**2012**) 144201.

[33] A. Brinkmann, A.P.M. Kentgens, Proton-Selective ^{17}O-^{1}H distance measurements in fast Magic-Angle-Spinning solid-state NMR spectroscopy for the determination of hydrogen bond lengths, *J. Am. Chem. Soc.* 128 (**2006**) 14758–14759. doi:10.1021/ja065415k.

[34] B. Hu, J. Trébosc, J.-P. Amoureux, Comparison of several hetero-nuclear dipolar recoupling NMR methods to be used in MAS HMQC/HSQC, *J. Magn. Reson.* 192 (**2008**) 112–122. doi:10.1016/j.jmr.2008.02.004.

[35] F.A. Perras, T.W. Goh, L.L. Wang, W. Huang, M. Pruski, Enhanced 1H-X D-HMQC performance through improved homonuclear decoupling; *Solid State Nucl. Magn. Reson.* 98 (**2019**) 12-18. doi.org/10.1016/j.ssnmr. 2019. 01.001

[36] R. Fu, S.A. Smith, G. Bodenhausen, Recoupling of heteronuclear dipolar interactions in solid state magic-angle spinning NMR by simultaneous frequency and amplitude modulation, *Chem. Phys. Lett.* 272 (**1997**) 361–369. doi:10.1016/S0009-2614(97)00537-X.

[37] J.A. Jarvis, I.M. Haies, P.T.F. Williamson, M. Carravetta, An efficient NMR method for the characterisation of ^{14}N sites through indirect ^{13}C detection, *Phys. Chem. Chem. Phys.* 15 (**2013**) 7613. doi:10.1039/c3cp50787d.

[38] G. Bodenhausen, R. Freeman, G.A. Morris, A simple pulse sequence for selective excitation in Fourier transform NMR, *J. Magn. Reson.* 23 (**1976**) 171–175. doi:10.1016/0022-2364(76)90150-5.

[39] G.A. Morris, R. Freeman, Selective excitation in Fourier transform nuclear magnetic resonance, *J. Magn. Reson.* 29 (**1978**) 433–462. doi:10.1016/0022-2364(78)90003-3.

[40] R. Freeman, Selective excitation in high-resolution NMR, *Chem. Rev.* 91 (**1991**) 1397–1412. doi:10.1021/cr00007a006.

[41] V. Vitzthum, M.A. Caporini, S. Ulzega, J. Trébosc, O. Lafon, J.-P. Amoureux, G. Bodenhausen, Uniform broadband excitation of crystallites in rotating solids using interleaved sequences of delays alternating with nutation, *J. Magn. Reson.* 223 (**2012**) 228–236. doi:10.1016/j.jmr.2012.05.024.

[42] D. Carnevale, V. Vitzthum, O. Lafon, J. Trébosc, J.-P. Amoureux, G. Bodenhausen, Broadband excitation in solid-state NMR of paramagnetic samples using Delays Alternating with Nutation for Tailored Excitation ('Para-DANTE'), *Chem. Phys. Lett.* 553 (**2012**) 68–76. doi:10.1016/j.cplett.2012.09.056.

[43] X. Lu, J. Trébosc, O. Lafon, D. Carnevale, S. Ulzega, G. Bodenhausen, J.-P. Amoureux, Broadband excitation in solid-state NMR using interleaved DANTE pulse trains with N pulses per rotor period, *J. Magn. Reson.* 236 (**2013**) 105–116. doi:10.1016/j.jmr.2013.09.003.

[44] B.E.G. Lucier, A.R. Reidel, R.W. Schurko, Multinuclear solid-state NMR of square-planar platinum complexes-cisplatine and related systems, *Can. J. Chem.*, 89 (**2011**) 919-937. doi:10.1139/V11-033.

[45] F.A. Perras, M. Pruski, Reducing t_1 noise through rapid scanning, *J. Magn. Reson.* 298 (**2019**) 31-34.

[46] M. Bak, J.T. Rasmussen, N.C. Nielsen, SIMPSON: A general simulation program for solid-state NMR spectroscopy, *J. Magn. Reson.* 147 (**2000**) 296–330. doi:10.1006/jmre.2000.2179.

[47] Z. Tošner, R. Andersen, B. Stevensson, M. Edén, N.C. Nielsen, T. Vosegaard, Computer-intensive simulation of solid-state NMR experiments using SIMPSON, *J. Magn. Reson.* 246 (**2014**) 79–93. doi:10.1016/j.jmr.2014.07.002.

[48] S.K. Zaremba, Good lattice points, discrepancy, and numerical integration. *Annali di Matematica Pura ed Applicata*. 4 (73), 293-317 doi:10.1007/BF02415091

[49] H. Conroy, Molecular Schrödinger Equation. VIII. A new method for the evaluation of multidimensional integrals, *J. Chem. Phys.* 47 (**1967**) 5307–5318. doi:10.1063/1.1701795.

[50] V.B. Cheng, H.H. Suzukawa, M. Wolfsberg, Investigations of a non-random numerical method for multidimensional integration, *J. Chem. Phys.* 59 (**1973**) 3992–3999. doi:10.1063/1.1680590.

[51] J. Herzfeld, A.E. Berger, Sideband intensities in NMR spectra of samples spinning at the magic angle, *J. Chem. Phys.* 73 (**1980**) 6021–6030. doi:10.1063/1.440136.